Corrosion behaviour of steel used in boilers for biomass combustion

Katarzyna Irena Siwek

Thesis to obtain the Master of Science Degree in

Energy Engineering and Management

Supervisor: Prof. Maria de Fátima Grilo da Costa Montemor

Examination Committee

Chairperson: Prof. Francisco Manuel da Silva Lemos

Supervisor: Prof. Maria de Fátima Grilo da Costa Montemor

Member of the Committee: Prof. Maria João Pedroso Carmezim

October 2015

Acknowledgments

This thesis is based on the work conducted within the KIC InnoEnergy Master School, in the MSc programme Clean Fossil and Alternative Fuels Energy. This programme is supported financially by the KIC InnoEnergy. The author also received financial support from KIC InnoEnergy, which is gratefully acknowledged.

KIC InnoEnergy is a company supported by the European Institute of Innovation and Technology (EIT), and has the mission of delivering commercial products and services, new businesses, innovators and entrepreneurs in the field of sustainable energy through the integration of higher education, research, entrepreneurs and business companies. Shareholders in KIC InnoEnergy are leading industries, research centres, universities and business schools from across Europe.

The MSc programme Clean Coal Technologies is a collaboration of:

AGH University of Science and Technology, Kraków, Poland,

SUT Silesian University of Technology, Gliwice, Poland

IST Instituto Superior Técnico, Lisbon, Portugal.

Acknowledgments

I would like to take the opportunity to thank the many people who have made this thesis possible.

Firstly, I wish to express my deepest gratitude and appreciation to Prof. Fátima Montemor my supervisor at (IST) for her proper guidance, dedication, and supervision throughout this project. This work would not have been successfully completed in this form without her valuable advices and constructive comments during many extensive discussions.

I am also thankful to dr hab. inż. Konrad Świerczek, my supervisor at AGH University of Science and Technology, for his suggestions and recommendation for improvement of the thesis.

Special thanks goes to Yegor Morozov (PhD student) for his encouragement and endless support throughout the research steps. His language corrections technical suggestions, and constructive advices were valuable guidance for keeping me on the right track. I am really grateful for his assistance whenever I had equipment difficulties and willingness to help no matter how much work he had additionally. I was really privileged to have him as my co-supervisor.

Moreover I want to thanks my colleagues at Electrochemical laboratory for sharing me numerous coffees, lunches, and good time. They always kept a cheerful and welcoming attitude.

Finally, I would to like to say thanks to my family and friends for their infinite emotional support , mostly to my boyfriend for his never-ending patience and motivation.

This dissertation was made in cooperation with *Metalerg* producer of organic straw-fired boilers from Oława (Poland), which provided material to analyze.

Abstract

The use of biomass, especially agricultural waste in heat and energy production is becoming more widespread worldwide due to its CO_2 neutrality and a lower cost if compered to fossil fuel. However, it is a heterogeneous fuel with a high amount of alkalis and chlorine which cause more corrosion problems than forest and fossil energy sources.

Although there is a great interest to reduce the costs associated with this phenomena very little has been reported in small-scale biomass boilers. The furnace walls and heat exchangers are those parts of boiler, which are subjected to high corrosion risk. The first ones are usually made of low carbon steel, due to its low price and good mechanical properties, while more corrosion resistant alloys, based on chromium and nickel, are generally considered for critical parts.

In this work, the variation in mass and scale thickness after oxidation in air and in presence of KCl at temperatures from 600ºC – 1100ºC have been determined and studied to explain the corrosion behaviour of carbon steel. Analyses of corrosion products by using optical microscopy, SEM, EDS and Raman were carried out to correlate mass change results with the composition and morphology of the corrosion products. Furthermore the corrosion resistance of the oxide scales formed was evaluated by d.c. potentiodynamic polarization in aqueous electrolytes at room temperature.

The results indicated that samples oxidized in air exhibits non-linear mass gain with the protective iron-oxide (Fe_3O_4 and Fe_2O_3) formed mainly at higher temperatures, while those in presence of salt resulted in mass loss driven by scale spallation. Thus, the surfaces attacked by aggressive molten species, which presence was confirmed by different analyses, were more susceptible to further oxidation-induced corrosion.

Results obtained in aqueous electrochemical tests revealed two sets of behaviours, with samples oxidised in air at higher temperatures being anodically polarised and thus more corrosion resistant compared to the ones oxidised at lower temperatures.

Key words: carbon steel, biomass boilers, high temperature corrosion, oxidation, potentiodynamic polarisation

Resumo

A utilização da biomassa e resíduos agrícolas, especialmente na produção de calor e energia, é cada vez mais usual em todo o mundo devido a emissões reduzidas de CO_2 e a um baixo custo comparativamente ao combustível fóssil. No entanto, trata-se de um combustível heterogéneo com uma elevada quantidade de álcalis e cloro que, por sua vez, causam mais problemas de corrosão relativamente às fontes de energia fósseis e florestais.

Embora haja um grande interesse para reduzir os custos associados a este fenómeno, muito pouco tem sido descrito em caldeiras de biomassa de pequena escala. As paredes da fornalha e dos permutadores de calor são as partes da caldeira que estão sujeitas a um risco de corrosão elevado. As primeiras são geralmente feitas de aço com baixo carbono, devido ao seu baixo preço e boas propriedades mecânicas, enquanto que as ligas mais sofisticadas baseadas em cromo e níquel são consideradas para as partes críticas.

Neste trabalho, a variação da espessura e da massa após oxidação em ar e oxidação na presença de cloreto de potássio a temperaturas seleccionadas foram estudadas e, por conseguinte, utilizadas para explicar a corrosão do aço carbono. A análise dos produtos de corrosão por meio de microscópia óptica, SEM, EDS e Raman foi realizada para, assim, correlacionar os resultados da variação da massa com a sua composição e morfologia. Além disso, a taxa de corrosão foi avaliada por polarização potenciodinâmica contínua.

Os resultados indicaram que as amostras oxidadas em ar apresentaram um ganho de massa não-linear devido ao óxido de ferro protector (Fe_3O_4 e Fe_2O_3) formado, principalmente, a temperaturas mais elevadas, enquanto que as amostras na presença de sal resultaram numa perda de massa impulsionada pela fragmentação superficial. Assim, as superfícies atacadas agressivamente, onde as espécies fundidas, cuja presença foi confirmada pelas diferentes análises, foram as mais susceptíveis à corrosão corrosão. Em meio aquoso verificou-se uma maior resistência à corrosão das amostras oxidadas a temperaturas mais elevadas que revelaram uma forte polarização anódica.

Palavras-chave: aço carbono, caldeiras de biomassa , corroção a alta temperatura, oxidação, polarização potenciodinamica

Content

List of Tables

List of Figures

Nomenclature

p_{O_2} – Partial pressure of oxygen [Pa]

p_{CO} – Partial pressure of carbon oxide [Pa]

p_{CO_2} – Partial pressure of carbon dioxide [Pa]

ΔG_T° – Standard Gibbs free energy change [J/mol]

R – Universal Gas Constant [8.3144 J/kg*K]

T – Temperature [°C] [K]

A – Area [mm^2]

Δm – Mass change [g]

SEM – Scanning Electron Microscopy

EDS – Electron Dispersive Spectroscopy

WDS – Wavelength-Dispersive Spectroscopy

SEs – Secondary electrons

BSE – Backscattered electrons

Introduction

Biomass utilization for energy and heat production has drawn much attention recently. The increase of biomass consumption is driven by either economic potential, seen in substantially growing fossil fuel prices or CO_2 neutrality of sustainable cultivated biomass. The latter refers to zero net carbon emission: plants absorb CO_2 during photosynthesis, which is later released during combustion. According to recent findings, the use of biomass for heat and power applications can reduce emissions by 55-98 % compared to today's fossil fuel mix in power generation [1].

In general, two main sectors are considered for biomass utilisation: energy-producing industry and small-scale heating applications. The first one involves large companies that make long-term investments and already have infrastructure to adopt biomass as a source of energy. The small-scale heating segment gets the advantage of a higher direct conversion efficiency than electricity – 80 % vs 35-40 % [1]. Depending on the application, biomass can provide the heat for an entire residence in much the same way as a conventional technology [3]. According to the diagram of primary fuels in the global energy supply (Figure 1), biomass covers approximately 10 % (52 EJ) of the global energy supply, of which two-thirds is used in developing countries for cooking and heating (34 EJ).

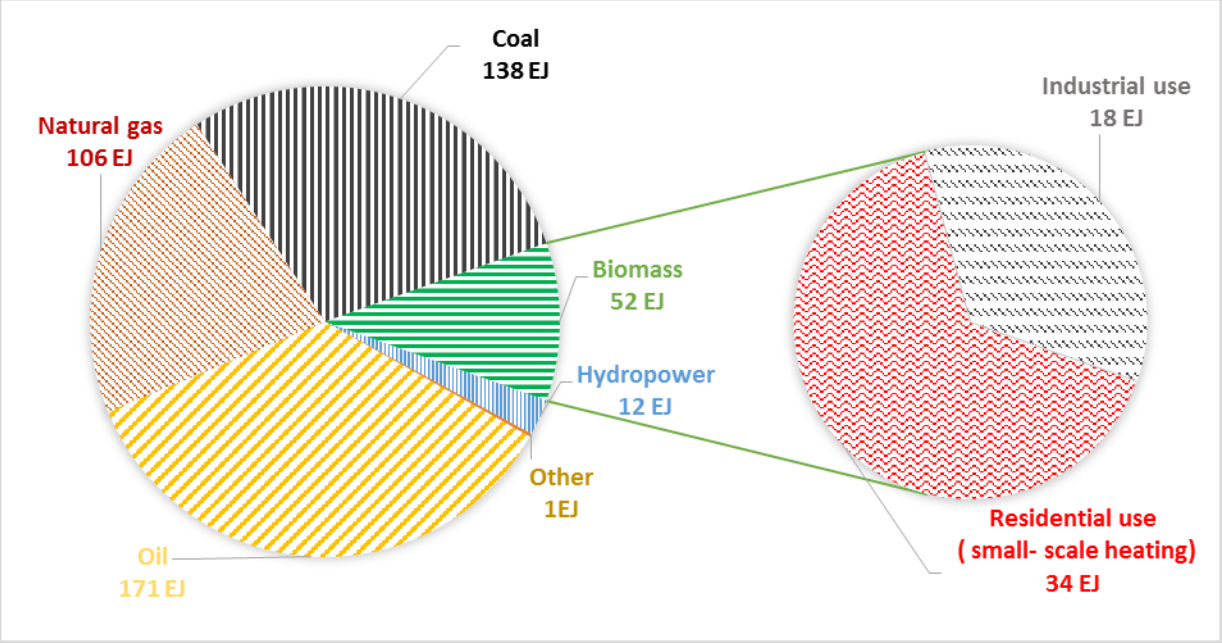

Figure 1. Global energy supply [2].

Aim and goals of the thesis

Therefore, the aim of the research work is the investigation of corrosion behaviour of low carbon steel during high-temperature corrosion in chloride-containing environment, typical for straw biomass boiler, in order to be able to justify (or not) its application as boiler structural material and to predict the corrosion performance depending on the operational conditions. The main objectives of the research were to examine and compare the performance of the considering steel under hot corrosion in oxidizing conditions both for air and chloride-rich environment, as well as estimate its relative corrosiveness in given conditions as a function of temperature and time. Typically these boilers are operated at temperatures from 600 to 700ºC and relevant changes in the corrosion process are likely to occur in this range, especially when KCl is present. Moreover, during shutdown, in the presence of humidity and aggressive species, other types of corrosion can occur and its detrimental effect has been scarcely studied. Thus, this MSc work intends to bring additional information, beyond the actual state-of-art.

1. Biomass as an alternative source of energy

Biomass is referred both to animal and plant-derived materials, but from the perspective of energy resources, only plant-derived biomass is considered, with particular characteristics that makes it different from fossil fuel. Though there is no established way of classifying biomass, from the viewpoint of application, it is categorized as forestry resources and agricultural waste. Such specification is essential for designing, operation and maintenance of the biomass combustion systems, as well as its operation and maintenance. Among these, wood and straw are available in large quantities and widely used as reliable feedstock for small-scale biomass boilers.

1.1 Biomass chemical composition and physical properties

Due to chemical composition and physical properties, biomass is regarded as demanding fuel from the viewpoint of involved technologies, revealing various handling problems and causing difficulties when combusted. Whereas forest biomass utilization is easier to manage, the use of agricultural waste for energy production faces a number of complications related to the high content of inorganic species.

Table 1 Physical properties of solid biomass and coal [4].

Parameter		Bituminous coal	Forest biomass	Non-forest biomass
Total moisture	wt. %	3.2 – 19.1	4.9 -68.5	6.1 – 41.0
Ash content	wt. %	3.5 – 26.9	0.3 – 6.9	1.3 – 16.3
Volatile matter	wt. %	29.39 – 35.86	70.67 – 82.83	52.67 – 80.38
Heating value	MJ/kg	21.08 – 27.66	4.39 – 19.38	13.19 – 24.79

In the table 1, biomass properties are compared with ones of coal. Biomass is characterised by higher moisture and volatile matter contents, but lower heating value and energy density. High moisture content causes lower adiabatic combustion temperature. Furthermore, the drying stage during the combustion becomes longer, so volatiles releasing and char combustion are delayed, often requiring larger furnace space. The optimal moisture content is found around 15%, although certain biomass furnaces can manage up to 65%.Furthermore, ash content is another guiding parameter for a boiler design.

The composition of biomass and its ash is dependent on the plant species and its life conditions as soil quality, fertilizers applied and nutrients available as well as weather conditions. Carbon, oxygen and hydrogen are the main constituents of any biomass. Due to the carbohydrate structure, biomass is highly oxygenated. Typically, 30-45 wt.% of the biomass dry matter is oxygen. Another principal constituent is carbon, making up from 30-60 wt.% depending on ash content. Hydrogen, together with carbon, determines the heating value of the fuel, and is a third major component of the biomass comprising typically to 5-7 wt.%. Nitrogen, sulphur, and chlorine can also be found in biomass, but their quantity normally is lower than 1 wt.%. Nitrogen is a main contributor for the formation of pollutant emissions, whereas sulphur and chlorine favour corrosion processes. Other inorganic elements such as Cl, P, K, Ca, Mg, Na, Si are always present too in trace amounts and considered as major ash forming elements,

and their ratio is relevant for the ash melting temperature. These components influence corrosive volatile gas creation and scales formation occurring during combustion processes [5].

1.1.1 Straw characteristic

In terms of aforementioned physical and chemical characteristics, straw is an agricultural waste with potential to be used as a feedstock for heat and energy production. It is a by-product resulting from the growing of commercial crops: wheat, barley and oat. Straw is considered as a low calorific combustible material (Table 2) with the net calorific value in a range of 13,5 – 19,0 MJ/kg depending on moisture content, which can be decreased by drying in the air. It is also characterised by high content of volatiles accounted for 80 % of total mass and low bulk density (50-120 kg m^{-3}). The letter one, apart from the transportation issues, reduces the heating value per unit volume and causes difficulties in continuous feeding and the control of the burning rate [11].

Table 2. Physical and chemical characteristics of wheat straw and wood. [6,7]

Parameters:		Wheat straw	Wood chips
Water content	[%]	14-20	40
Volatile components	[%]	>70	>70
Ash	[%]	3	0.6-1.5
Carbon	[%]	43	50
Hydrogen	[%]	5.2	6
Oxygen	[%]	38	43
Nitrogen	[%]	0.41	0.3
Sulphur	[%]	0.10	0.05
Chloride	[%]	0.2	0.02
Potassium	[%]	1.01	-
Calorific Value, Water/Ash-free	[MJ/kg]	18.7	19.4
Ash softening temperature	[°C]	950-1100	1000-1400
Ash composition			
SiO_2	[%]	59.9	11.6
Al_2O_3	[%]	0.8	2.0
K_2O	[%]	16.9	9.2
Na_2O	[%]	0.4	0.6
CaO	[%]	7.3	40
MgO	[%]	1.8	4.8
P_2O_5	[%]	2.3	4.4
Fe_2O_3	[%]	0.5	1.8
Other	[%]	10.1	25.6

Wheat straw contains less carbon, oxygen and hydrogen than woody biomass, but the amount of minor elements such as chloride (0.2 wt.%), potassium (1.1 wt.%) and sulphur (0.1 wt.%) is significantly higher. The quality of feedstock is primarily determined by an ash content, which varies in both sources, being about 3-10 wt.% for wheat. SiO_2 (60 wt.%) is its main component, while CaO comprises 40 wt.% of wood ashes. K_2O is the other main element in wheat straw and wood accounted for 17 % and 9 % respectively.

The high silica content influences the feed quality, whereas alkali metals reduces an ash melting temperature. In general, the higher the fuel alkali and chlorine contents, the lower are the sintering temperatures.

1.2 The biomass combustion process

Fuel properties and the manner by which they affect the combustion are fundamental issues for boiler design and process control. Combustion is a multi-stage process that involves simultaneously occurring heterogeneous and homogeneous physical and chemical reactions [9]. The general chemical reaction involved in the combustion of biomass in air can be presented as following [10]:

$$C_aH_bO_cN_dS_eCl_fSi_gP_hM_i \cdot yH_2O + \ air\ (O_2 + N_2)$$

$$\rightarrow intermediates\ (char, tars\ and\ gases, mainly\ CO, CO_2, H_2, C_mH_n) + air$$

$$\rightarrow CO_2 + CH_4 + CO + C + H_2O + NO_2 + N_2O + NO + SO_2 + HCl + MCl_x + M_2(SO_4)_x + \cdots,$$

where M – metals (K, Ca, Mg, Zn, etc.)

The combustion process consists of four basic stages, such as drying (moisture evaporation), de-volatilisation (thermal decomposition or gasification), char combustion and gas phase oxidation. Each stage results in a different set of chemical compounds being formed. The contribution of the stages in overall process depends on the fuel size and properties, combustion process conditions as well as technology implemented.

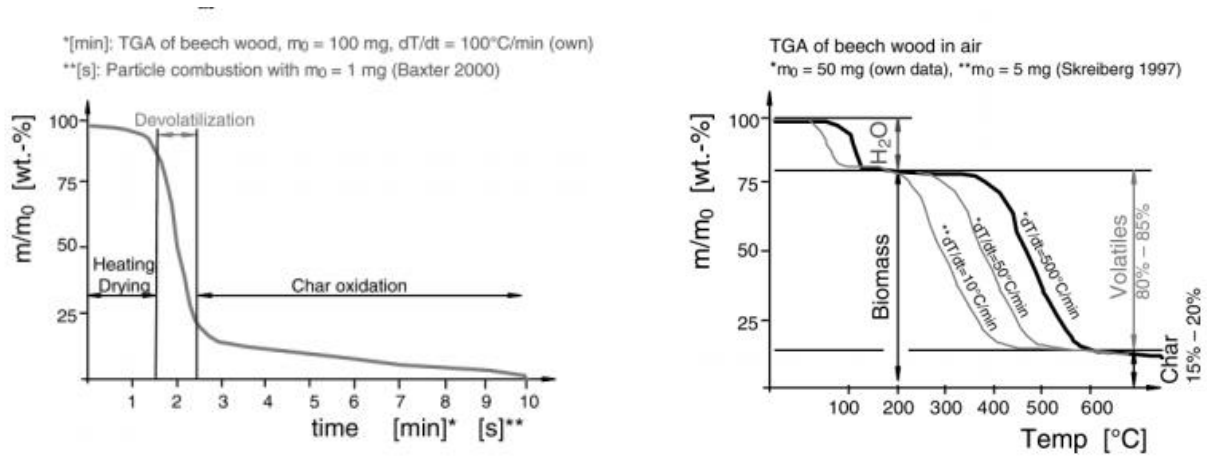

a b

Figure 2. Mass loss as a function of time (a) and temperature (b) during combustion of wood [9].

The drying stage occurs at temperatures close to 100°C (Figure 2) and is an endothermic step, which consumes energy released in other stages of the combustion process. If the content of moisture exceeds 65 % the combustion in conventional boilers, with fixed grate, cannot be sustained since a significant amount of energy is required. The de-volatilisation stage starts at 200°C and its rate increases, reaching the maximum at 300-400°C, decreasing then as the volatile matter is driven off, and finally a prompt

decrease at 400-500°C is observed. Volatiles released are combusted in gas phase oxidation reaction, creating a flame and generating considerable amount of energy. The gas phase reaction is highly exothermic with a rate being expressed as a function of temperature, pressure and concentration of volatiles and oxygen. Char remaining after de-volatilisation is burnt in char combustion stage producing CO_2, ash and heat [26].

During drying and de-volatilisation stages, hydrocarbons, CO, CO_2 and H_2O, as well as some inorganic compounds, such as alkalis, HCl, KCl, SO_2, K_2SO_4, etc. are released. As the temperature increases, the composition can change, as seen from Figure 3. It has been suggested that the alkali compounds start releasing at relatively low temperatures (200-400°C) in the form of KCl dust together with HCl (g). The HCl concentration increases, reaching the maximum at 730°C due to chemical conversion of KCl with SO_2 in presence of oxygen to form HCl and K_2SO_4, which follows the HCl trend in the mid-temperature range (530 -770°C). However, most of the potassium is evaporated in the form of KCl (g) between 700-830°C. At higher temperatures (830-1000°C) potassium can be also released in form of KOH [13].

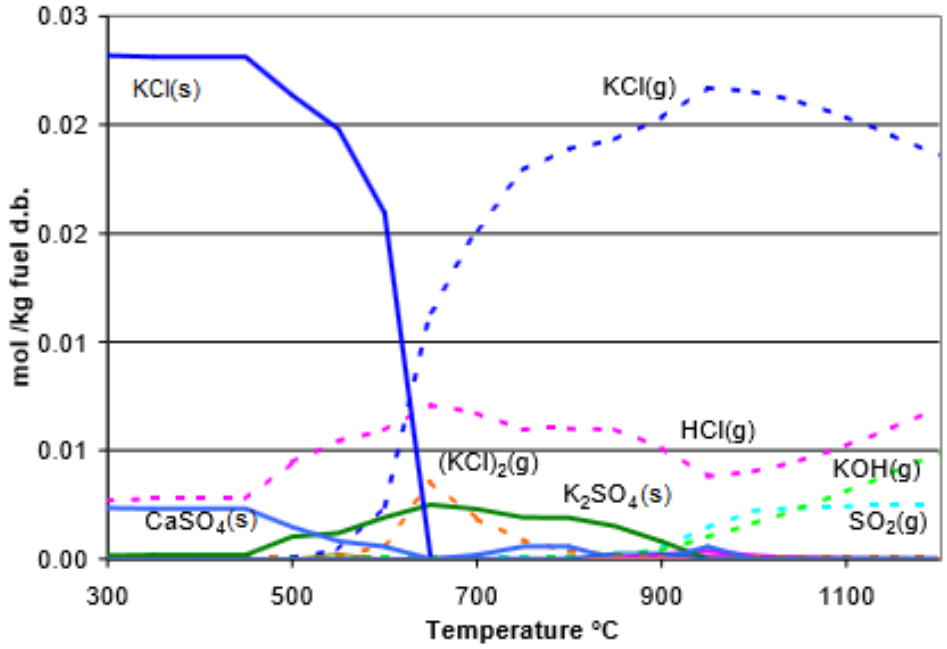

Figure 3. Chemical equilibrium for relevant ash forming elements in the flue gas passing a straw-fired boiler [12].

2. Biomass combustion technologies

Biomass boilers are available with a broad range of power output from several kW to several hundred MW. The diversity of biomass feedstock as well as its various properties influence combustion technology development. Generally, a typical boiler consists of grate and combustion chamber lined with a high temperature resistant ceramic material. There are two principal approaches applied for biomass grate design, namely fixed grates and moving grates. The first one is appropriate for biomass

fuel with considerably low moisture content (20-25%), whereas moving grate is suitable for wet feedstock (40-60%) [14]. Apart from them, boilers with fluidised bed systems are good alternatives for large-scale applications. Fluidised bed boilers burn effectively poor quality biofuels, sustaining low emission level. However, the current large-scale biomass combustion is mainly done by co-firing with coal.

2.1 Small-scale technologies for straw combustion

The conventional combustion equipment is not appropriate for burning agricultural residues such as straw. Typically, batch-fired boilers (Figure 4) are implemented for straw combustion due to their simplicity of use, possibility of mixing of different biomass fuel as well as for economic reasons. The power achieved for straw combustors ranges from 20 to 1000 kW. According to the new standards, its working principle is based on counter combustion air staging technologies. This solution results in both high efficiency (70-80%) and high temperature with complete burnout. All batch-fired boilers are equipped with combustion air fans controlled by an electronic unit. The flue gas temperature and oxygen content are used as control parameters. The proper temperature is additionally secured by refractory linings of firebricks round the walls of the chamber.

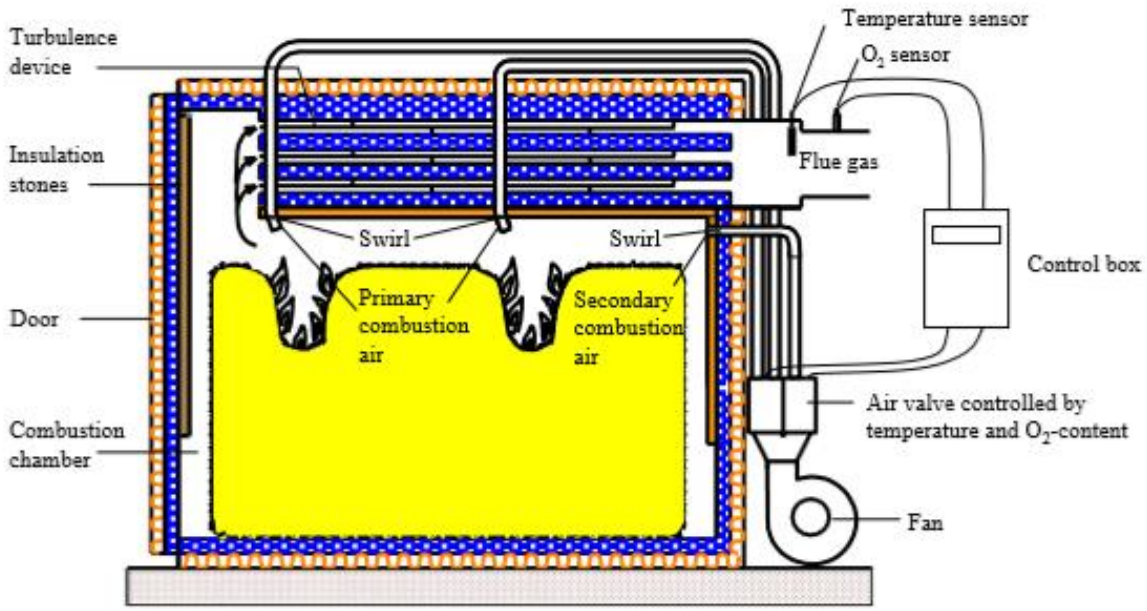

Figure 4. Schematic representation of a typical batch straw boiler produced in Denmark [15].

2.2 Materials selection for boilers production

The materials used for production of biomass combustion boilers have their limitations, mainly due to the high-temperatures involved, and the solution to the heat related problems is primarily the compromise between careful material selection, process control and better boiler design, but the ultimate choice is usually based on accessibility and a price [16]. Various metal alloys are the best

candidates with strength and high temperature resistance being key issues. Carbon steels, nickel-alloy steels and stainless steels are the most commonly used materials.

Carbon steel is an alloy of iron and carbon, which is added to increase the hardness and strength. Other certain elements as silicon, phosphorus, sulphur and manganese are also present (< 0.5 % Si, < 1.5% Mn) . For carbon steels, the carbon content is in range of 0.12-2.0 %; they can be classified into low carbon steels (<0.3 %), medium (0.3-0.9 %) and high carbon steels (0.9-2.0 %) [17]. The increase of the carbon concentration leads to the decrease of the melting temperature, as seen from phase diagram Fe-C (Figure 5).

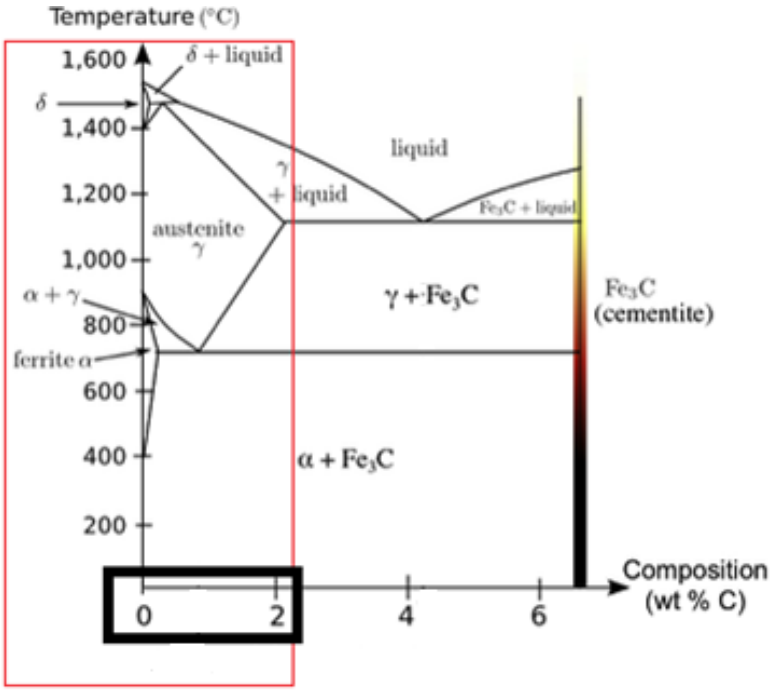

Figure 5. Fe-C phase diagram [22]

Whenever more aggressive environments are involved, nickel-base alloys and stainless steels are the materials to be selected. Nickel improves toughness, ductility and weldability of steel. Nickel-base alloys show higher resistance towards aggressive conditions compared to carbon steels. They are also characterized by higher service temperatures (Figure 6). Moreover, the addition of chromium (10 % or greater) provides resistance resulting from the formation of a protective Cr_2O_3 surface oxide layer [18,19]. The latter materials to be considered are stainless steels. They are divided into four main types depending on their microstructure: ferritic, martensitic, austenitic and duplex stainless steels. For this type of steels the carbon content must be low, (<0.2 %) to sustain performance in aggressive environment. Under high temperature conditions, carbon can diffuse to the grain boundaries and precipitates chromium carbide, which lowers the chromium content in the solid solution [20].

The most common stainless steel is the 304 grade (8 % Ni and 18 % Cr). It has good strength and ductility, but also provides resistance in moderately oxidizing atmosphere. When extra corrosion resistance is required, 316 (16-18 % Cr, and 10-14 % Ni) and 310 type (24-26 % Cr, and 19-22 % Ni) austenitic steels are used. 316 has similar composition to 304, but 3% of molybdenum is to improve the

corrosion resistance in chloride-rich environment [18]. On the other hand, 316 stainless steel is prone to catastrophic oxidation at temperature above 770°C due to volatility of MoO_3 and further creation of low-melting eutectics [21].

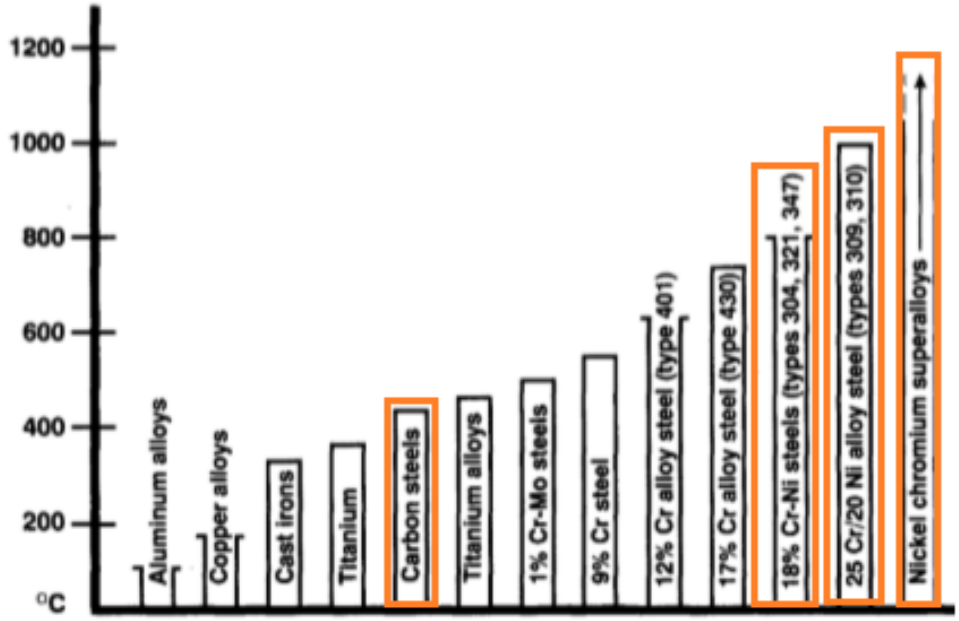

Figure 6. Maximum service temperatures of common engineering materials suggested for oxidation in clear air or oxygen [16]

In addition, it was found that advanced nickel-based high strength alloys can be also used in boilers manufacturing. They are traditionally composed of nickel (>50%) and chromium. Elements such as molybdenum, tungsten, cobalt or titanium are added to confer additional strengthening, since increasing of Cr content leads to a decline of mechanical properties. Type 625 (58%Ni, 20%Cr, 8%Mo) and 671 (52%Ni, 48%Cr, 0.4% Ti) are more resistant to corrosion both in reducing and oxidazing environments compared to standard stainless steels but are considerably more expensive (Figure 7) [16,21].

Boiler walls and other structural elements are traditionally manufactured from carbon steels, primarily from low carbon ones. This material is relatively cheap, highly available and provides good mechanical properties, but is not as robust at high temperatures as other alloys. This problem could be solved by optimised boiler design. An increase in wall thickness, as well as application of refractory lining are common practices to improve the service life. Stainless steels and nickel based alloys, on the other hand, are considered for the critical parts of boilers, e.g. heat exchangers, super-heaters (steam boilers), which are subjected to aggressive conditions [21]. The last mentioned is used as outer cladding material for coextruded tubes of heat exchange surfaces.

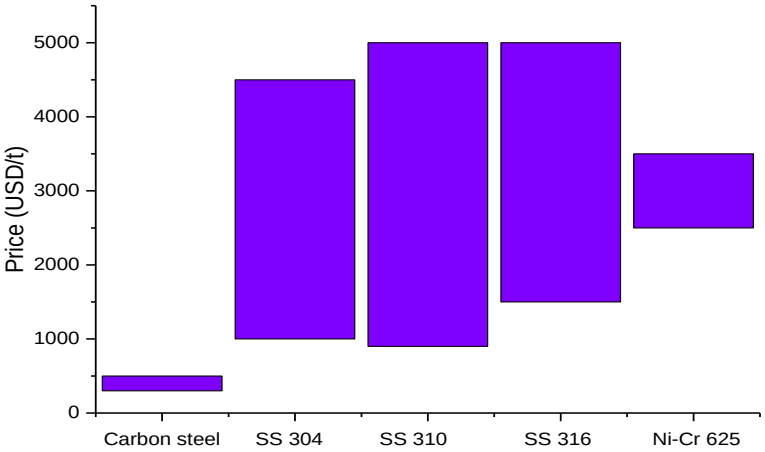

Figure 7. Price per tonne of selected materials [24].

3. Hot temperature corrosion

Hot temperature corrosion refers to the degradation processes of metallic material caused by chemical attack from gaseous, liquid and solid products formed, for example, in thermal units. Those products react with each other during combustion and with exposed metal due to the presence of defects in the protective metal oxides, leading to further metal damage. Corrosion of the furnace walls and critical parts of boiler may lead to loss in material thickness up to 1mm/year, whereas oxidation processes in air, in the same range of working temperatures takes place at slower rates - around 100 μm/year.

High temperature corrosion, as hot temperature degradation process, plays a pivotal role in the selection of materials for industrial equipment as mentioned in section 2.2. Different environments and principal modes, for instance: oxidation, sulfidation, carburization and nitration are summarized schematically in Figure 8. Oxidation is the most important process, often taking place in high temperature processes, regardless of the predominant mode in both oxidizing and reducing environment, being controlled by the oxygen contents. In fact metallic alloys, often relay on this process to develop protective oxide scales to resist sulfidation, carburization and ash/salt deposition corrosion. Lowering the oxygen activity in presence of high sulphur potential tends to make an environment more sulfurizing, so that sulfidation mechanism is dominant. Either carburization and nitration behave in similar manner with decreasing oxygen activity. The same reactions become more severe when the environment is reducing [23].

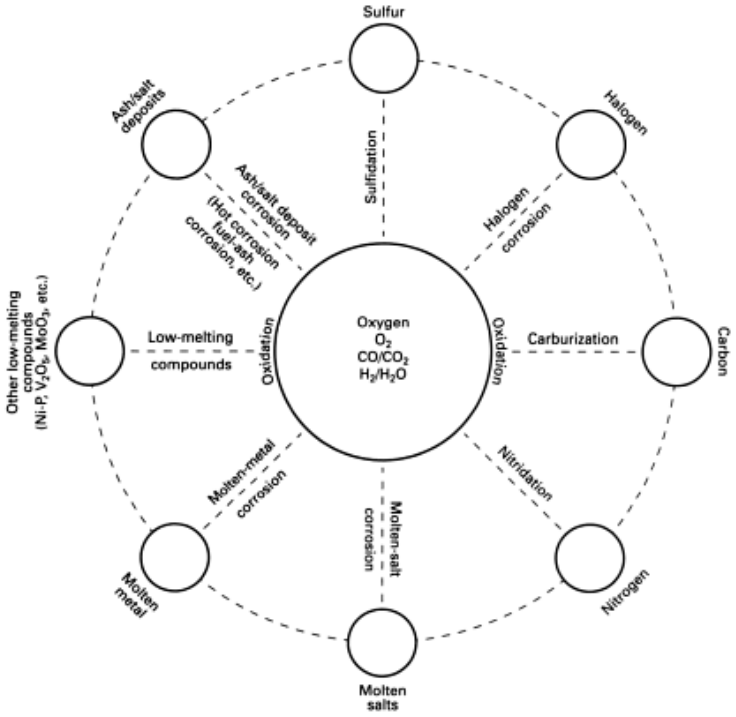

Figure 8. Diagram showing all modes of high-temperature corrosion with their corrosive reactants [23].

3.1 Thermodynamics

The basic criterion governing the ability of a metal to undergo oxidation under specific conditions is a negative change in the standard free energy (ΔG_T^o) of the process below:

$$aM_{(s)} + \left(\frac{b}{2}\right) O_{2(g)} = M_b O_{a(s)} \quad (1)$$

Considering reaction 1, an oxide is formed over the metal surface when the oxygen potential is greater than the oxygen partial pressure in equilibrium with the oxide [25]. The equilibrium oxygen partial pressure is known from the standard Gibbs energy of the oxide formation (eq. 2):

$$p_{O_2} = exp\left(\frac{-\Delta G_T^\circ}{RT}\right) \quad (2)$$

Thus, if no oxygen is involved in further oxide formation the oxide might be reduced to the metallic form when reducing agents are available (e.g. CO or CO_2). In these conditions, the oxygen potential can be controlled, for example by the ratio: P_{CO}/P_{CO2}, according to the reaction:

$$2CO + O_2 = 2CO_2 \quad (3)$$

and the corresponding equation for oxygen partial pressure is presented as following:

$$p_{O_2} = \frac{exp(-\Delta G_T{}^o/RT)}{(p_{CO}/p_{CO_2})^2} \quad (4)$$

Since both oxidizing and reducing combustion atmospheres can be present in a boiler, knowledge about oxygen partial pressure as well as CO/CO_2 ratio is relevant in terms of selecting the alloying elements used for the alloy manufacturing. Apart from the above formulas, the metal behaviour can be determined

directly from Ellingham diagram (Figure 10). The diagram is a visualization of the relative stability of metals and their oxidized products expressed in $\Delta G°$ per mole of O_2 as a function of temperature. Generally, when the temperature increases, the standard free energy of formation is less negative, resulting in lower oxide stability. For this reason, basic alloying metals such as Fe or Ni form the oxides which are less stable than ones created by other metals (Cr, Mn).

Iron as one from a few metals can develop several oxides $FeO/Fe_3O_4/Fe_2O_3$ from the innermost to the most outer respectively. Each one will dissociate at different pressures and the oxide that is richer in oxygen will usually dissociate to an oxide containing less oxygen not to a metal directly, consequently the innermost layer becomes the thickest one. According to Ellingham diagram the interface Fe_3O_4/Fe_2O_3 reaches an equilibrium with the gas under an oxygen partial pressure of 10^{-6} atmosphere (atm), at higher pressures the reaction proceeds to form hematite (Fe_2O_3). However, when the partial pressure of oxygen decreases, hematite is decomposed and magnetite (Fe_3O_4) is formed [27]. Similar situation occurs where the lines $FeO \rightarrow Fe_3O_4$ and $Fe \rightarrow FeO$ intersect, below 570°C (indicated by the red line in Figure 8). FeO is unstable and decomposes to iron and Fe_3O_4 resulting in presence of just two oxide layers.

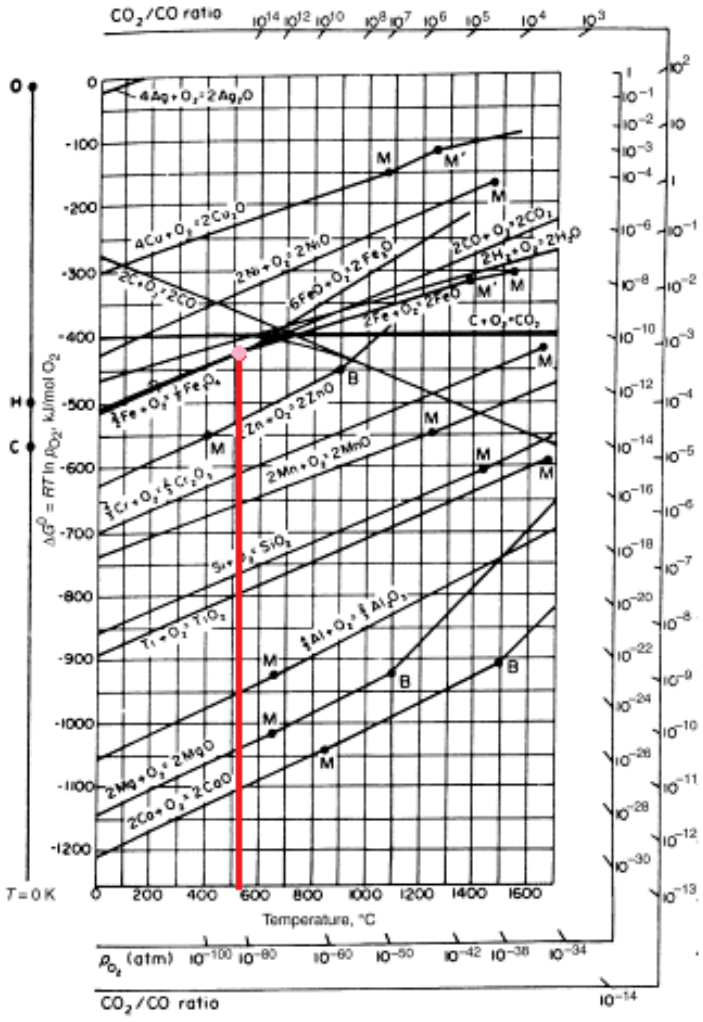

Figure 9. Ellingham diagram for various oxides created during oxidation process from the main alloying elements; M – melting point of metal, B-boiling point of metal, M' – melting point of metal [29].

3.2 Oxide film properties

The first stage in a metal-oxygen reaction involves the adsorption of gas on the metal surface. The adsorbed oxygen dissolves into the metal forming a thin continuous film of its oxide that may protect the underlying surface.

In practice, protectiveness of formed oxide scale may be determined by Pilling-Bedworth (PB) relationship between the volumes of oxide produced and oxide consumed. If the oxide is insufficient to fully cover the metal, the PB ratio is found lower than 1 (porous, volatile), which is not effective in blocking oxygen from the surface. PB ratio slightly higher than 1 (continuous) should be protective without cracks and pores due to a control of compressive stresses in oxide layer. In certain conditions, oxides with volume much greater than the volume of metal (PB ratio>>2) cause developing excessive stresses, that can lead to complete breakdown of the scale [29,30]. The Table 3 groups metal oxides according to their P-B ratios.

Table 3. Properties of metal oxides important for mild, stainless and nickel based steels [29,30]

Protective metal	Metal oxide	R_{BP}	Non-protective metal	Metal oxide	R_{BP}
Al	Al_2O_3	1.28	Ca	CaO	0.64
Ni	NiO	1.65	Mg	MgO	0.81
Fe	FeO	1.77	Mn	MnO_2	2.37
Cr	Cr_2O_3	2.01	Mo	MoO_3	3.27

3.3 Kinetics of oxidation process

The analysis of reaction kinetics, apart from the previously described thermodynamics, is essential to obtain a comprehensive view of scale formation on the metal. Generally, the kinetics of oxidation obey to one of various possible oxidation models: parabolic, linear and logarithmic as shown in Figure 10. The first one is found at all temperatures, includes a diffusion controlled step, responsible for the maintenance of a thick coherent layer. The linear dependency may be observed during initial exposure times, at higher temperatures and when the oxide grows on the metal surface, the barrier oxidation layer does not provide protection due to oxide cracking, volatile oxide or presence of molten products. The last mentioned kinetic model was found at very low temperatures and is not relevant in high temperature engineering problems.

Most metals and engineering alloys follow the parabolic rate (Cr, Ni, Fe), however some minor metals with linear oxidation kinetics such as molybdenum, tungsten, or vanadium are added to increase

material properties. For these alloys the oxides begin to grow at a rate that decreases with time, which corresponds to the parabolic rate, but above a critical temperature it accelerates linearly due to oxide volatility resulting in catastrophic oxidation. Similar phenomena can be observed when a liquid phase is formed in the process. For example, on mild steel exposed to KCl at temperature higher than its melting point, the solid scales lose adherence after liquid phase penetration. The transition from parabolic to linear rate is also observed for mild steel oxidized in air. At lower temperature the rate of the process follows a parabolic rate, and when the temperature rises above 750°C it suffers rapid oxidation exhibiting a linear rate evolution. Unlike the mild steel, both chromium and nickel based alloys (stainless steel and Ni-Cr Inconel alloys respectively) show very negligible oxidation rate at temperatures up to 700°C; thus the parabolic kinetic model describes the whole process. Further additions of chromium to the alloys improves even more the oxidation resistance [31].

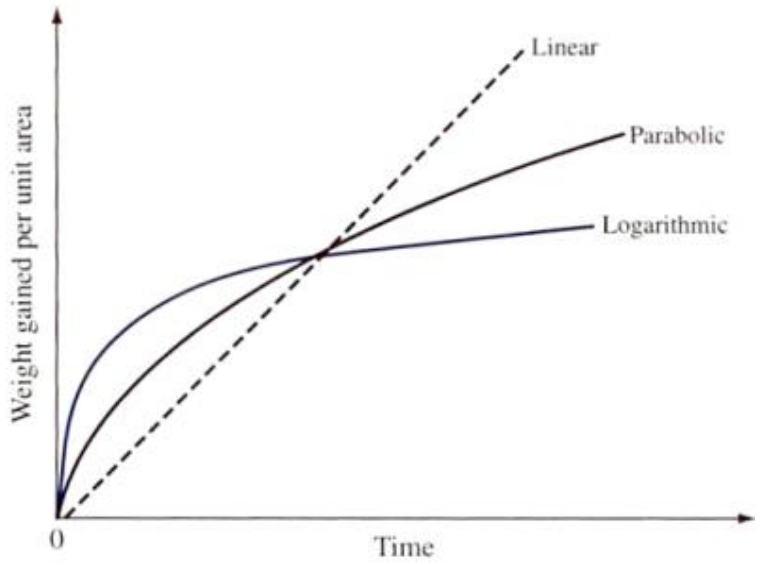

Figure 10. Oxidation kinetics for linear, parabolic and logarithmic oxidation [32].

3.4 Structural metal corrosion induced by Cl-species

Hot temperature corrosion of steel in chloride-rich environments, which is a typical one in boilers, is a complicated phenomenon caused by oxygen, water and chlorine-containing agents. The speed of the corrosion and the products formed are in direct dependence on the ratio between these species and the nature of the bare metal.

On carbon steel, the main reaction taking place is the reaction of formation of iron oxide film eq. (5 and 6), which leads to a rather uniform scale that protects the metal from further oxidation. However, the corrosion can become catastrophic in the presence of chlorides. Chloride and chlorine-containing species, either in gaseous state (HCl, Cl_2), liquid (molten salts such as KCl) or solid state (ash), become involved in the process eq. (7-10, 12-15) and can attack the bare metal and/or iron oxide film.

$$3Fe_{(s)} + 2O_{2(g)} \rightarrow Fe_3O_{4(s)} \quad (5)$$

$$4Fe_{(s)} + 3O_{2(g)} \rightarrow 2Fe_2O_{3(s)} \quad (6)$$

$$2HCl_{(g)} + 0.5O_{2(g)} \leftrightarrows Cl_{2(g)} + H_2O_{(g)} \quad (7)$$

$$Fe_{(s)} + Cl_{2(g)} \rightarrow FeCl_{2(s)} \quad (8)$$

$$Fe_{(s)} + HCl_{(g)} \rightarrow FeCl_{2(s)} + H_{2(g)} \quad (9)$$

$$H_{2(g)} + Cl_{2(g)} \rightarrow HCl_{(g)} \quad (10)$$

$$2H_{2(g)} + O_{2(g)} \rightarrow H_2O_{(g)} \quad (11)$$

$$FeCl_{2(s)} \rightarrow FeCl_{2(g)} \quad (12)$$

$$3FeCl_{2(g)} + 2O_{2(g)} \rightarrow Fe_3O_{4(s)} + 3Cl_{2(g)} \quad (13)$$

$$2FeCl_{2(g)} + 1.5O_{2(g)} \rightarrow Fe_2O_{3(s)} + 2Cl_{2(g)} \quad (14)$$

$$2KCl_{(s,l)} + Fe_2O_{3(s)} + 0.5O_{2(g)} \rightarrow K_2Fe_2O_{4(s)} + Cl_{2(g)} \quad (15)$$

Gas phase corrosion attack can be initiated by HCl and Cl_2. Cl_2 is normally present at higher temperatures in absence of moisture eq. (7). It penetrates into the protective oxide layer by diffusion, and through pores and cracks, reaching the scale-metal interface, where it reacts with the metal eq. (8) to form chlorides. A similar process occurs with HCl eq. (9) that forms iron chlorides, which are volatile and leave the interface in the form of iron chloride alone eq. (12) or together with KCl. At higher temperatures, this can cause the delamination and decomposition of the oxide layer. In an O_2-Cl_2 environment, the stability of the metal oxides and chlorides depend on the partial pressures of oxygen and chlorine as shown in Fe-eq Cl-O system (Figure 11). Chlorides are stable at low oxygen partial pressures, typical found at the metal/scale interface, whereas oxides are expected in the outer parts of scale, where higher oxygen pressures are observed. Films formed in such environment are porous, thus providing only limited protection. As iron chloride reaches the oxygen-rich surface, further transformation occurs eq. (13, 14), releasing chlorine and iron oxides, which however are not forming a film, since they appear from a gas phase and not as the result of the interface reactions (5,6). Most of the Cl_2 released eq. (13, 14) travels to the bulk gas, where it is converted to HCl eq. (7, 10), while remaining fraction migrates back to react with the metal and form metal chlorides again [33,34].

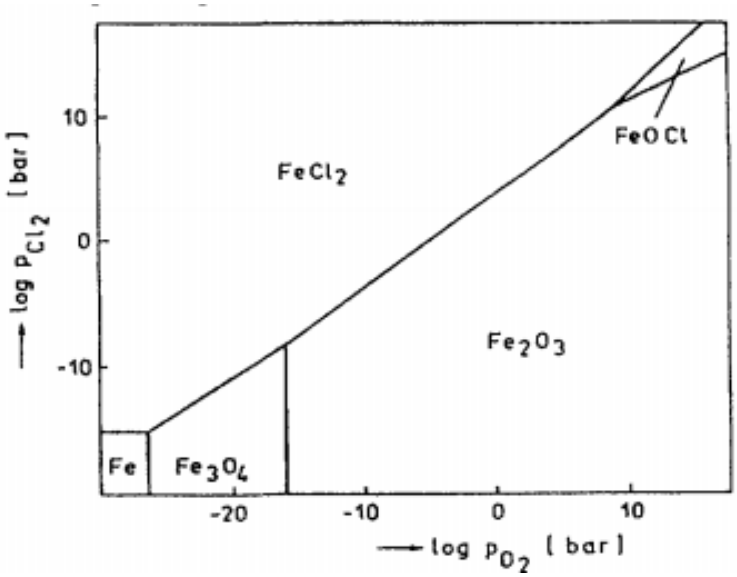

Figure 11. Phase diagram of the system Fe-O-Cl at T=833 K [34].

Another type of corrosion attack can take place in the presence of molten salts, with a main contribution from KCl, which can be in solid phase or melted, being in this condition much more aggressive. It can attack the oxide film in the presence of oxygen eq. (15), leading to the formation of cracked and porous scales, thereby contributing to the hot corrosion process. The species formed, $FeCl_2$/$FeCl_3$ can form eutectics with KCl resulting in considerably lower melting points (350°C for $FeCl_2$ and 220°C for $FeCl_3$), as shown in the binary-system diagrams (Figure 12a and 12b). The flux formed is an ideal environment for corrosion, acting as a solvent for corrosion products, which no longer can form a protective film.

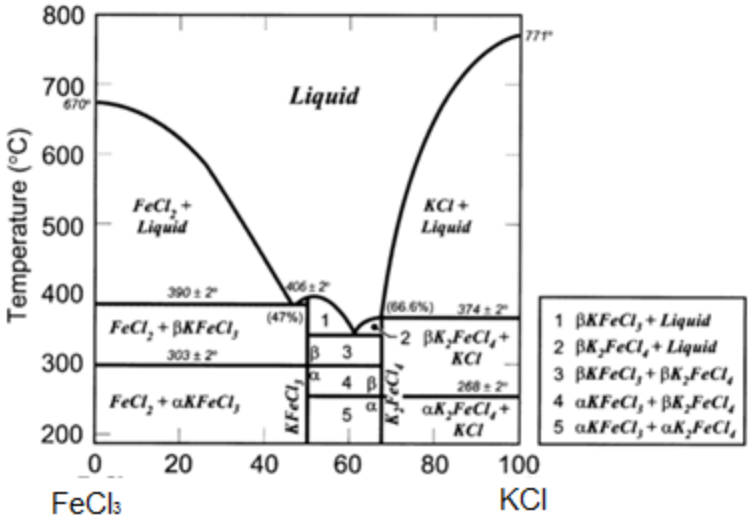

Figure 12a. Binary phase diagram of KCl–$FeCl_2$ [33].

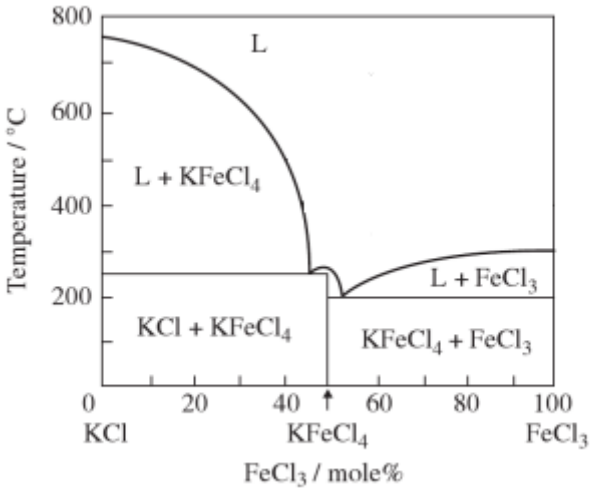

Figure 12b. Binary phase diagram of KCl–$FeCl_3$ [35].

Further, increase in temperature with time leads to evaporation of KCl and the transformation of iron chlorides into oxides in presence of oxygen eq. (13, 14).

The proposed mechanism can explain completely different behaviour of a steel during hot temperature corrosion in oxygen-rich environment in cases when aggressive species are presented or not.

4. Corrosion prevention in boilers

Two approaches are typically considered to prevent corrosion in boilers: one involves an improvement of the operating conditions to obtain less corrosive environments, and the other one is focused on the use advanced corrosion resistant materials.

The first one can be achieved either by the control of the flue gas parameters (oxygen content, temperature, humidity), or by the modification of the boiler design. The latter include changes in the exhaust flow configuration to promote good mixing along with flue gas recirculation as well as usage of protective ceramic linings.

Considering the boiler walls protection, usually at least first combustion chamber is lined with refractory elements with the extension to the top of second combustion chamber. Refractory usage varies from cast-aluminium oxide-based cements, having low heat transfer capability to highly engineered silicon carbide-based cements and special shapes with specific heat transfer characteristics [36].

As for corrosion resistant materials, double tubing design is the main approach. In such case, the inner layer is made from low carbon steel, the most common boiler material, while the outer part is high alloy steel (stainless or Ni-Cr), as discussed in Section 3.4. In addition, many manufactures improve corrosion resistance of materials by applying resistant coatings. Thermal spray methods have developed greatly during the last decades, and especially high velocity oxy-fuel method has improved to produce coatings with low porosity and high adhesion [37].

In order to find the best combination to provide protections against corrosion, significant findings in laboratory and field corrosion tests should be analysed. Thus, it is essential to understand the corrosion processes of these materials either in the absence and presence of KCl. There is also significant knowledge gaps when high temperature oxidizing environments contaminated with KCl are concerned.

5. Experimental

5.1 Material and samples preparation

In this study a low carbon steel, type P235GH, with the chemical composition given in Table 4, was used. It was provided by Metalerg, producer of biomass boilers (Poland), in the form of massive rectangular plates, additionally covered with a thin black layer resulted from high-temperature pre-treatment. They were cut to obtain small (ca. 15x15x10 mm) specimens and then polished (all sides) on LaboPol-25 machine with 180 and 500 silica carbide abrasive papers under water. The samples were dried and kept in acetone to prevent from its direct contact with air before testing. After that, the samples were dried and tests performed.

Table 4. Chemical Composition of EN 10028 P235GH [40].

Element	% by mass	Element	% by mass
Carbon (C)	≤0.16	Silicon (Si)	≤0.35
Manganese (Mn)	0.60 to 1.20	Phosphorous (P) (max)	0.025
Sulphur (S) (max)	0.015	Aluminium (Al)	≤0.020
Nitrogen (N)	≤0.012	Chromium (Cr)	≤0.30
Copper (Cu)	≤0.30	Molybdenum (Mo)	≤0.08
Niobium (Nb)	≤0.020	Nickel (Ni)	≤0.30
Titanium (Ti) (max)	0.03	Vanadium (Vi)	≤0.02

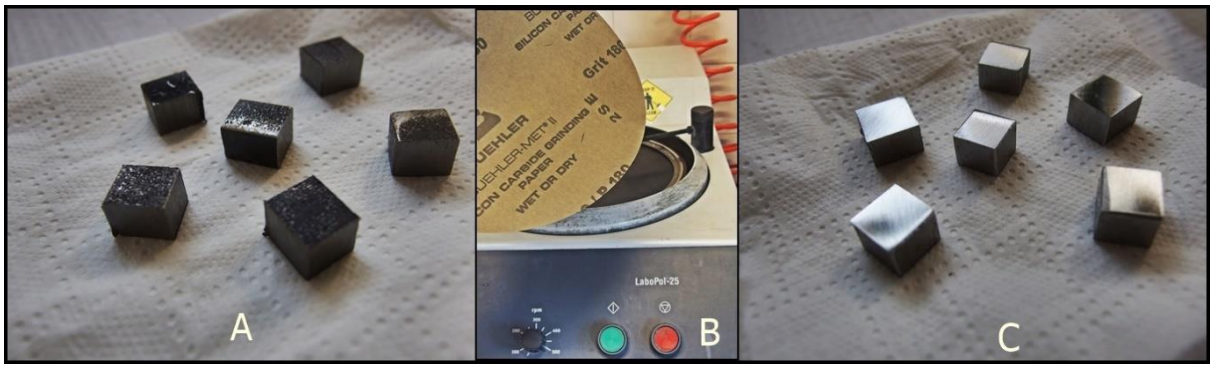

Figure 13. A – Steel specimens in as-received condition after cutting; B – Polishing paper and LaboPol- 25 machine; C – polished steel specimens.

Deionized water was used to prepare solutions used in electrochemical tests. All the chemicals (KCl, KOH, $KHCO_3$ and H_3BO_3) are all of analytical grade, purchased from Sigma-Aldrich.

5.2 Oxidation experiments

Hot temperature corrosion studies were performed under two different oxidation conditions, using a horizontal tubular furnace (Heraeus RE 2.1) consisting of a ceramic tube of 75 mm (internal diameter) and Thermicon P digital program controller (Figure 14). In order to place the samples, extra ceramic tube of 45 mm (internal diameter) was utilized.

The first set of samples was exposed to high temperature oxidation in air, while the second one was performed in the presence of potassium chloride, simulating an aggressive environment.

Figure 14. Setup for oxidation experiments.

5.1.1 Oxidation in air, without contaminants

Eight batches of three samples were used to perform first test at temperatures of 600, 800, 1000 and 1100°C for 48 and 72 hours in free air flowing environment. Such temperature selection was based on possible conditions occurring inside the biomass boiler. Prior oxidation, each specimen was weighted by a digital balance (Mettler AE166) with a precision of 0,0001 g, and its dimensions measured with a ruler with a precision of 0.5 mm, followed by placing the samples in high temperature resistant ceramic pots (Figure 15). After the test, the samples were cooled down inside the furnace and weighted again to estimate mass difference.

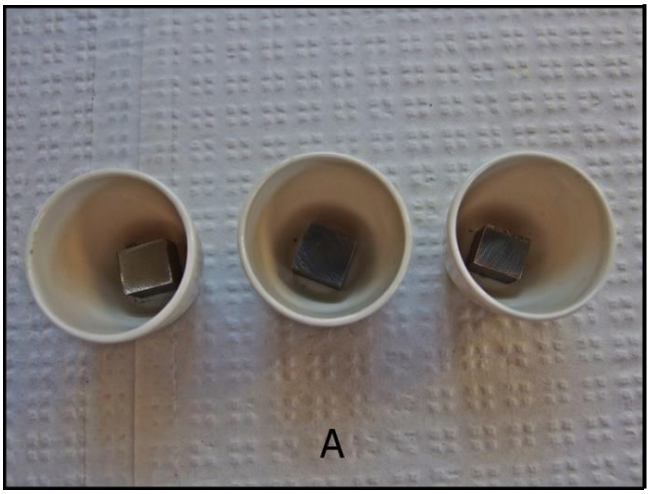

Figure 15. A. The samples placed in ceramic pots and positioned in the furnace.

5.1.2 Oxidation in air in the presence of KCl

In the second test, the oxidation in presence of the KCl salt was carried out. Potassium chloride was selected since it is the most abundant corrosion-active component of the straw ash. Six batches of three samples at temperatures were tested under 600, 800, 1000°C under for 2 and 3 days of exposure. The samples were processed in the same manner as in the first test, with the only difference that they were covered with KCl prior exposure at high temperature (Figure 16B).

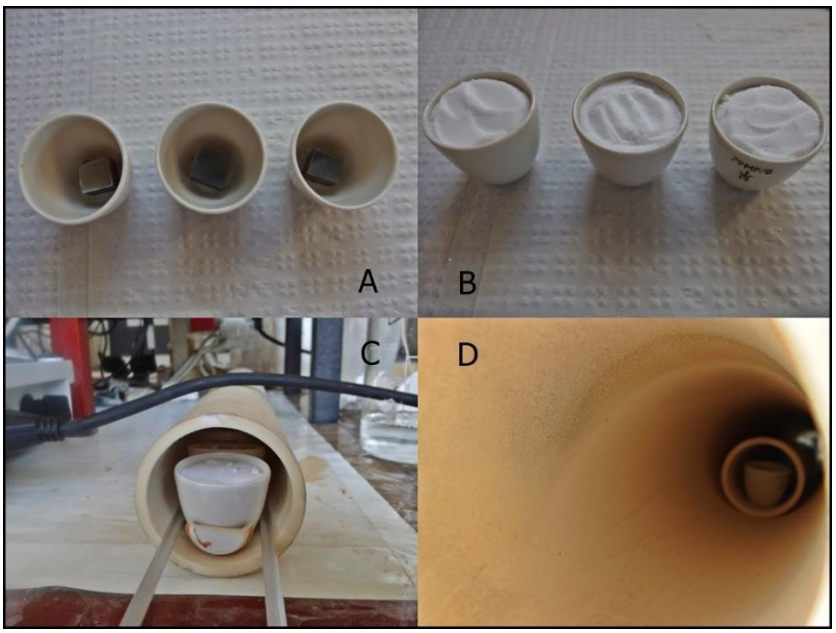

Figure 16. Samples preparation for oxidation in salt experiment.

To obtain expected mass loss the samples were cleaned from the salt remnants present on the surface, by dissolving it in distilled water. Each specimen was immersed in a beaker filled in the water which was heated to 60°C and maintained at this temperature for 10 minutes with simultaneous stirring on a magnetic stirrer (Figure 17). Finally the samples were dried in an oven at 40°C for 20 minutes and weighted.

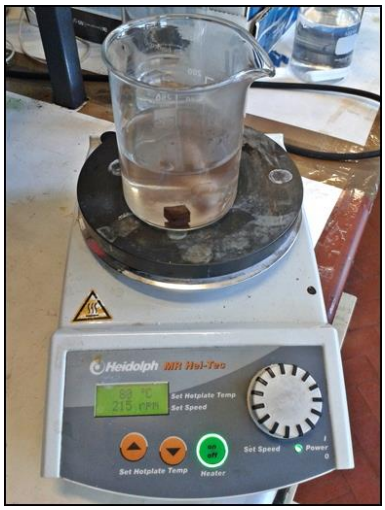

Figure 17. Salt removing process carried out with magnetic stirrer.

5.2 Electrochemical testing

There are many different electrochemical techniques used in corrosion science, however linear polarization (LPR) has been selected in the current work since it is the most common rapid quantitative technique to estimate the corrosion resistance and corrosion rate of metallic materials in a selected liquid environment.

It provides a current-potential relationship by reading the current response under linearly varied applied potential. One of the key parameters obtained is the corrosion potential (E_{CORR}), which is defined as the point where the current densities for anodic and cathodic reactions occurring on the surface of the specimen are equal being the corrosion current (I_{CORR}). The nearby region is known as the Tafel one and the corresponding slope can be used to estimate the polarization resistance and the corrosion rate. The test begins by applying a potential to the specimen, slightly more negative (cathodic) than E_{CORR}. The voltage is then increased until it reaches the E_{CORR}. Then, the test proceeds into the more anodic ($E > E_{CORR}$) potentials. After the corrosion potential has been surpassed, the specimen may undergo general or localized corrosion, depending upon the difference between E_{CORR} and the potential applied [42], the shape of the curve and the absence or presence of a breakdown potential, respectively. If the plotted graph has well defined linear regions, the corrosion rate can be calculated from I_{CORR}, otherwise less accurate qualitative approaches based on current-potential dependency should be used in order to assess the corrosion resistance.

LPR tests were performed using samples previously oxidized in different hot corrosion tests. Two identical samples were tested for each condition. Additionally, the LPR was carried out on raw steel as reference material. In order to prepare the samples for LPR, the rear side of the sample was abraded with the silicon carbide paper (180 and 500) and a wire connection was applied using conductive silver-based paint, the sample was placed then into Plexiglas mold and filled with epoxy resin (Gurit SP106), leaving the face side as received after hot corrosion test (Figure 18).

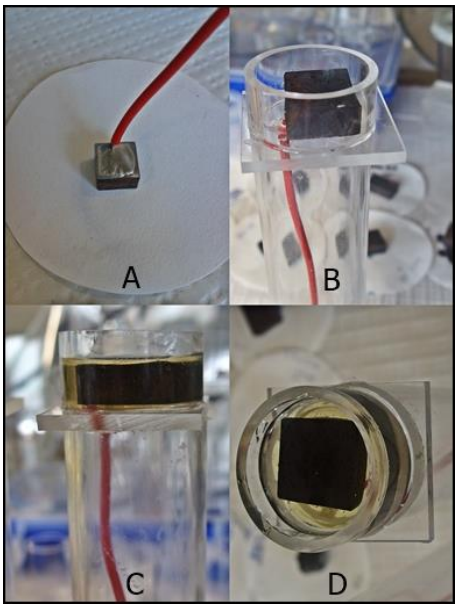

Figure 18. Sample preparation for the electrochemical test.

All electrochemical measurements employed a conventional three electrode electrochemical cell consisting of the steel sample as the working electrode (WE), Pt coil as the counter electrode (CE) and saturated calomel electrode (Hanna Instruments 5412) as the reference electrode (RE) (Figure 19A). The LPR tests were carried out in a Faraday cage at 25°C using potentiostat-galvanostat Autolab 302N interfaced with Nova 1.10 software (Figure 19B) with the potential sweep of 0.5 mV/s in the range from -350 to 350 mV vs open circuit potential (OCP). The polarization tests were carried out in a solution borate buffer solution of pH 9.4 (37.275 g/l KCl, 1.660 g/l KOH, 2.100 g/l $KHCO_3$, 3.092 g/l H_3BO_3) to mimic the environment inside a biomass boiler during the shutdown time when condensation is likely to occur. The data obtained was area normalized, plotted in the form of potential vs. current density logarithm curve and Tafel analysis was performed.

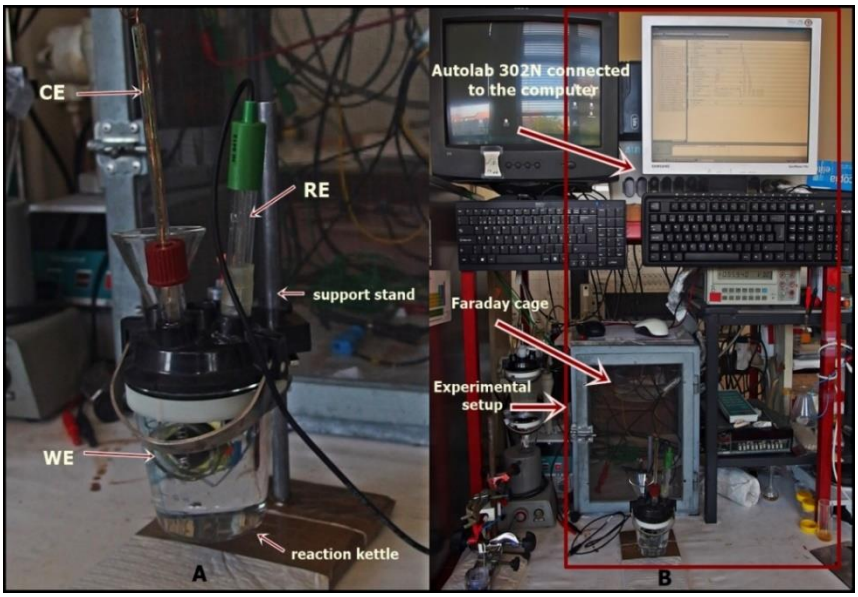

Figure 19. A. Electrochemical cell B. Experimental setup consisting of Autolab 302N potentiostat connected to the computer and Faraday cage.

5.3 Surface characterisation

Morphology and chemical composition studies were performed after the hot corrosion test. Optical microscopy, secondary electron microscopy (SEM) and Raman spectroscopy were used.

Optical microscope Leica DMS300 compatible with LAS ES software were used to record the surface morphology of the samples subjected to hot corrosion test at the macroscale. Additionally thickness of the scales was studied using cross-section samples to estimate the corrosion rate supporting the results of mass difference measurements.

The scanning electron microscopy, often coupled with different detectors, is a powerful tool for the material characterisation. It offers much higher spatial resolution (1-100 nm), as well as providing elemental analysis of the surface of a wide range of materials. A SEM image is generated by a focused electron beam that scans over the surface of the sample. During this interaction, mainly secondary electrons (SEs) and backscattered electrons (BSE) are released. The first ones are emitted from the atoms occupying the top surface and produce high-resolution images that reveal the sample morphology. The letter ones (BSE) are primary electrons that have been scattered elastically by atoms in solid providing information on variations in material composition. Heavier elements appear brighter than lighter ones in a backscattered electron image. Other signals include X-rays, which result from inelastic collisions of the incident electrons with other electrons in discrete orbitals of atoms [39]. Electron dispersive (EDS) or wavelength dispersive (WDS) X-ray spectroscopy detectors involve the identification of a specific energy or wavelength for rapid qualitative and quantitative elemental composition with a sampling depth of 1-2 microns. They may also be used to form maps or line profiles, showing the elemental distribution in a sample surface.

Several samples, namely samples from both hot corrosion tests at 600, 800, 1000°C, were selected for SEM investigation. Electron microscopy was performed with a JEOL 7001-F device equipped with field emission gun and an Oxford INCA unit for energy dispersive X-ray spectroscopy to carry out elemental analysis of the selected region. Images were obtained in secondary electrons and back-scattered electrons mode of topography and cross-section, which were complemented with chemical analysis.

Raman spectroscopy is a commonly used spectroscopic technique to provide the information about chemical composition of the system under investigation. It relies on inelastic scattering of monochromatic light that interacts with molecular vibrations and rotations, phonons or other excitations in the system, resulting in the energy of the laser photons being shifted up or down. The shift in energy is analysed then and the conclusion over chemical composition is made.

The Raman spectra of the corrosion products formed on the samples specified previously for SEM analysis were measured using LabRam HR Evolution Raman Microspectrometer (Jobin Yvon Horiba Scientific) equipped with a high stability Olympus BH2 microscope (Figure 20) for estimation of localized chemical composition. The excitation laser wavelength of 532 nm was employed and the spectra were collected over the range of 100 cm^{-1}–3200 cm^{-1} with a spectral resolution of 4 cm^{-1}.

Figure 20. LabRam HR Evolution Raman Spectrometer (left); objective 50X focused on the sample (right).

6. Results and discussion

The results of the experiments of oxidation in air and oxidation in the presence of KCl include both quantitative and qualitative assessment of the oxide scales formed on P235GH carbon steel at all the tested temperatures. The results are presented in the form of graphs for mass and thickness change (the later only for oxidation in air), as a function of temperature, for different exposure times. These experimental findings were supported by photographic evidences, as well as SEM/EDS and Raman analyses of samples at selected oxidation conditions. Furthermore, the corrosion susceptibility of the scales formed during oxidation were evaluated, in aqueous media by d.c. potentiodynamic polarization.

6.1 Oxidation in air

6.1.1 Mass and thickness change and micrographic analysis of the surface

It has been reported that the most efficient way to estimate the performance of a material in an oxidizing environment is to consider its mass change per unit of surface area in the corresponding conditions. As a matter of fact, in the case of a ferrous substrate the reaction between oxygen and iron results in mass gain of the exposed specimen with increasing temperature and exposure time [41]. These observations were confirmed in the measurements presented in Figure 21, which are consistent with the changes observed in the thickness of the formed scales (Figure 22) and morphological changes depicted in Figure 23.

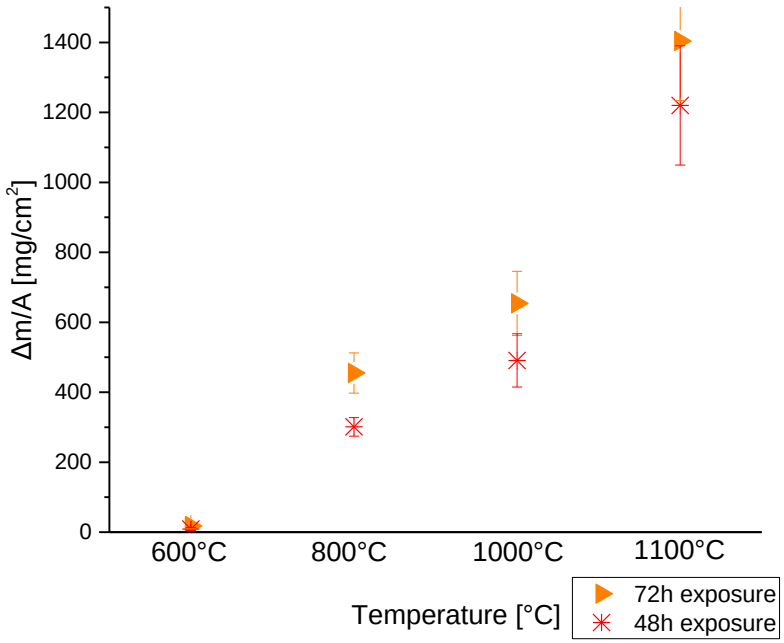

Figure 21. Mass gain per unit area (Δm/A) as a function of temperature of P235GH carbon steel during non-isothermal oxidation in air.

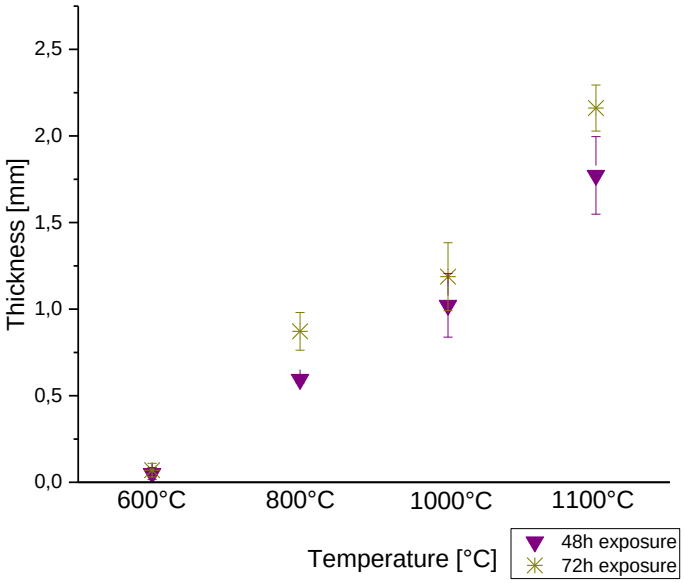

Figure 22. Scale thickness as a function of temperature of P235GH carbon steel during non-isothermal oxidation in air.

After both 48 and 72 hours of exposure at 600°C, there is a small mass gain along with the formation of a thin layer (<0,1mm). The layer was examined with an optical microscope and the result revealed a flaky structure with spalling material (Figure 23A and 23B), which according to literature can appear during cooling and are more pronounced on thinner film [42]. However it is difficult to determine whether it was created throughout the experiment or after, during cooling. At the higher temperatures, the mass change of the tested steel increased significantly from two to three orders of magnitude and of spalling was less evident at 800°C compared to 600ºC and it was not found at 1000 °C and over. The anomaly in the pattern was noted at 1100°C, which is a temperature much higher than the current operating range for biomass boilers. In this condition, the scale thickness was doubled if compared to 1000°C and its average value was 1,7 and 2,2 mm for 48 and 72 hours, respectively. This correlates well with the observations from the mass change calculations, but is rather difficult to explain. As noticed previously, when the temperature increased, the surface morphology changed to more compact at 800°C with dark and light coloured islands formed in the ferrous matrix as shown in Figure 23C and 23D. Those heterogeneities on the surface were less evident at 1000°C, temperature at which the homogenous scale appeared. At 1100°C a uniform and smooth oxide coating was fully developed (Figure 23G and 23H).

The increase in the mass gain and the corresponding changes in the surface morphology at temperatures above 600°C can be explained by faster diffusion of iron and oxygen ions that are affected both by the increasing temperature and porosity of the scale (confirmed with electron microscopy) [43]. The scale formed at higher temperatures is constituted by a layered structure of iron oxides with composition and microstructure changes from the substrate through the internal layers to the outer surface. The scale is thick and uniform externally, but brittle inside as revealed when some of the oxidized samples were subjected to mechanical work (polishing), which caused scale breakdown

(Figure 24). This type of delamination, was enhanced by the mechanical forces and it was the result of stresses occurring within the oxide and causing internal deformation due to the specific volume of the growing oxide not being the same as the volume of consumed metal in the reaction (Piling-Bedworth ratio) [44]. Furthermore, fallowing both the mass gain and variations in scale thickness for both exposure times it can be concluded that oxidation rate is clearly not linear. Non-linearity can indicate, that scale growth might be controlled either by chemical reaction between substrates or their diffusion trough porous structure. However, due to limited data is not possible to confirm it as well as determinate the actual kinetic model.

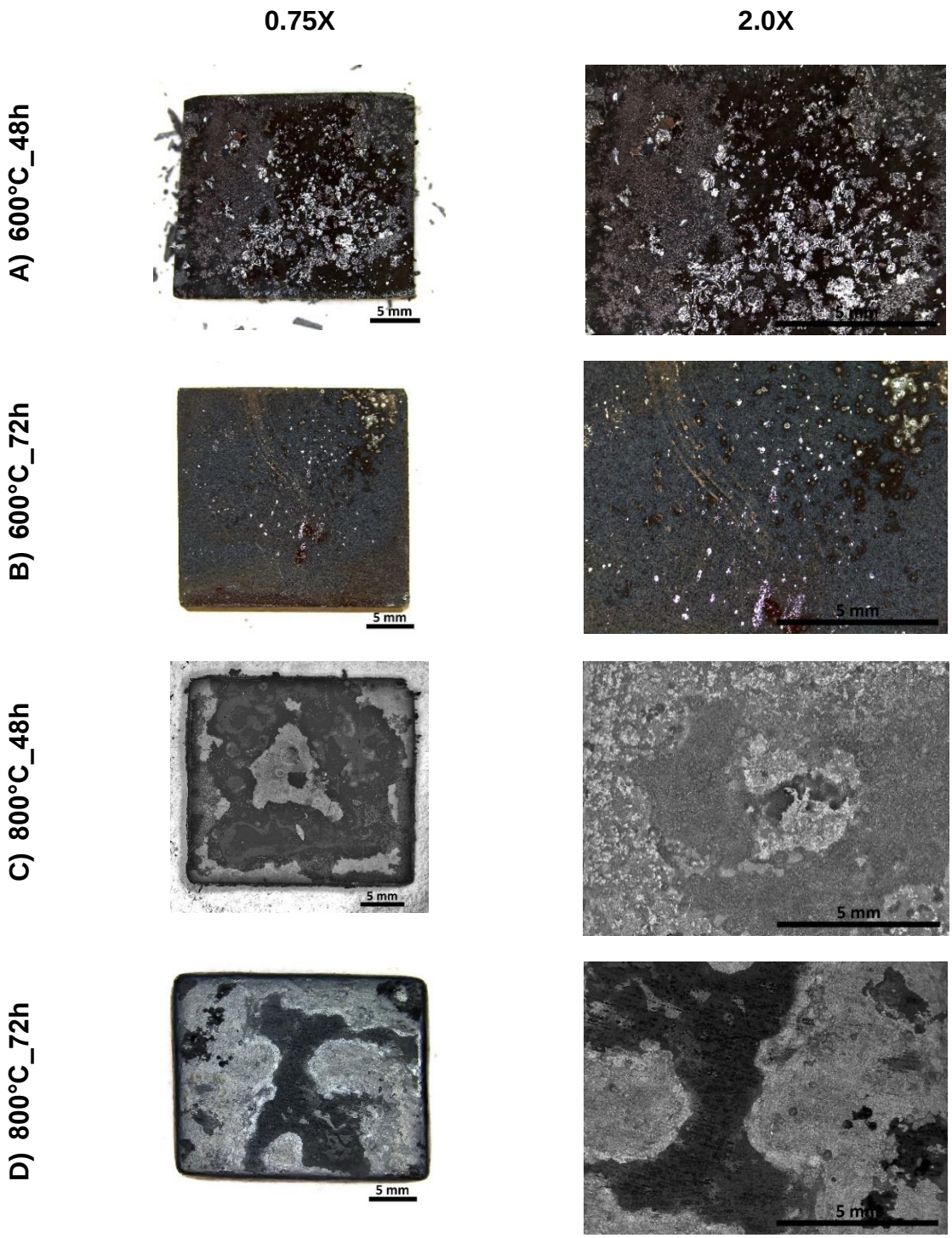

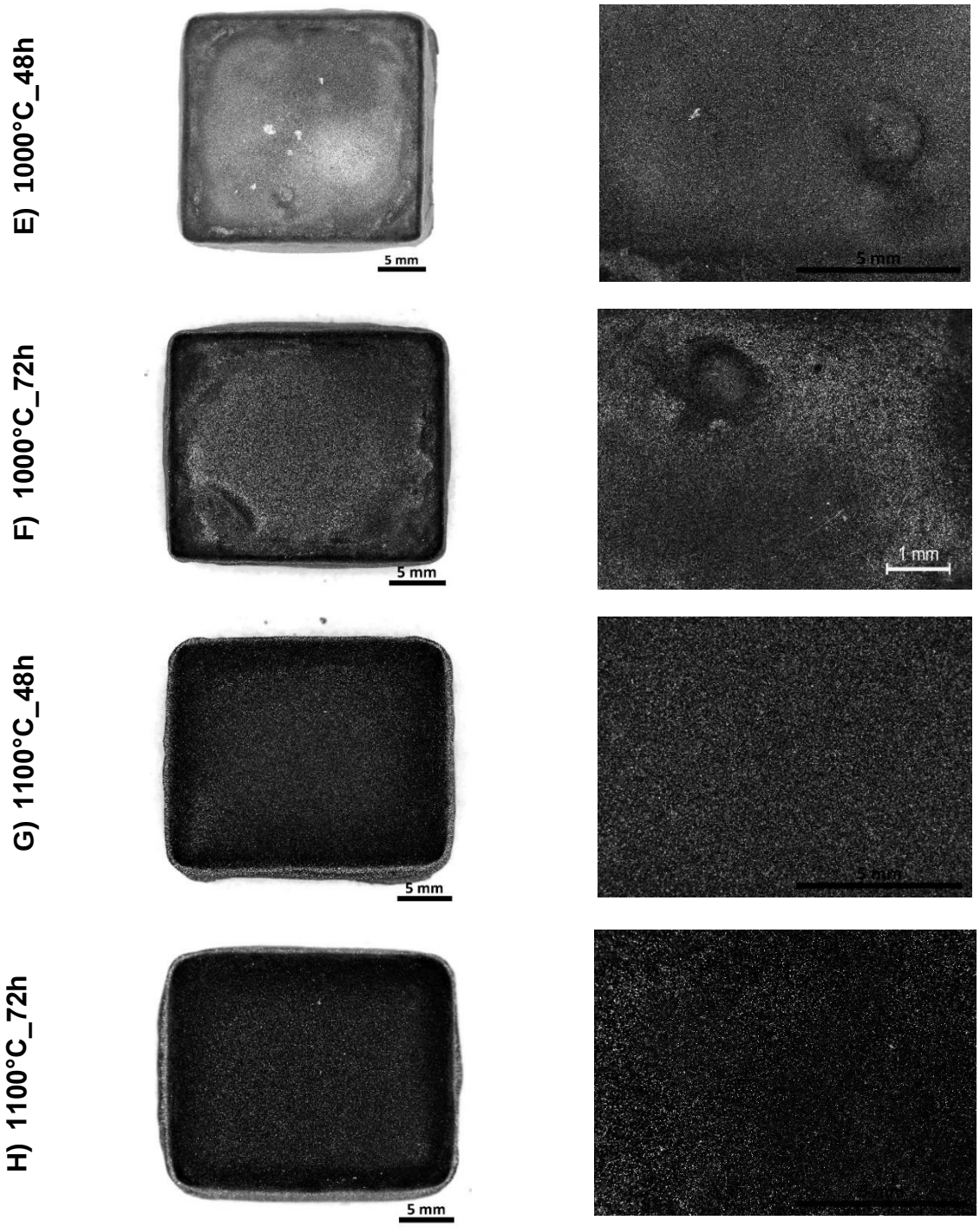

Figure 23. Optical micrographs showing the carbon steel after 48h and 72h of exposure at selected temperatures. The images were taken at 0,75X (left) and 2,0X (right) magnifications.

Figure 24. Examples of scale breakdown after oxidation at 800°C for 72h hours (left) and 1100°C for 48 hours (right).

6.1.2 Morphological and chemical identification of the scales

The analytical examination and chemical identification of the scales formed during oxidation for 48 h were mainly performed on specimens oxidized at 600 and 800 °C, which reflect the most likely conditions occurring inside the boiler. The SEM was primarily used to capture images of the products, while the EDS scan was performed in order to characterize the elements present on the product layer. Since the EDS only detects the chemical elements present in the scales, further identification was accomplished by Raman, where the obtained spectra were compare with the ones of iron oxides, because the corrosion products of carbon steel are well known to consist mainly of iron oxide compounds.

In the case of oxidation at 600°C the outer surface presented irregular fleecy structure (Figure 25a) with many needles detected (Figure 25d). In the literature similar needle-like shape were related to presence of goethite (FeOOH), while the fleecy ones indicate the presence of hematite [45]. Although, hematite is an expected product of oxidation, goethite also forms through the weathering of iron-rich materials [46]. At 800°C the aforementioned formations almost disappeared and only a few regions with needles were preserved as shown in Figure 26C and 26D. It clearly seen that, the morphology of the layer is not compact, contains many porous areas, which may indicate the occurrence of internal oxidation. On the other hand, the appearance of these areas and much lower amount of carbon identified with the EDS detector, compared to 600°C, can be also attributed to the decarburization of the steel at higher temperatures. During this process a significant amount of carbon diffuses to the surface and reacts with oxygen. The result of this reaction is the evolution of gaseous CO_2 and CO and the development of appreciable pressures beneath the scale, which in turn lead to the formation of cracks that were identified in cross-sectional SEM micrographs (Figure 28) [41]. The findings presented in Figure 28D and the other mentioned factors were responsible for partially delamination of the scales that occurred after exposure at 800°C.

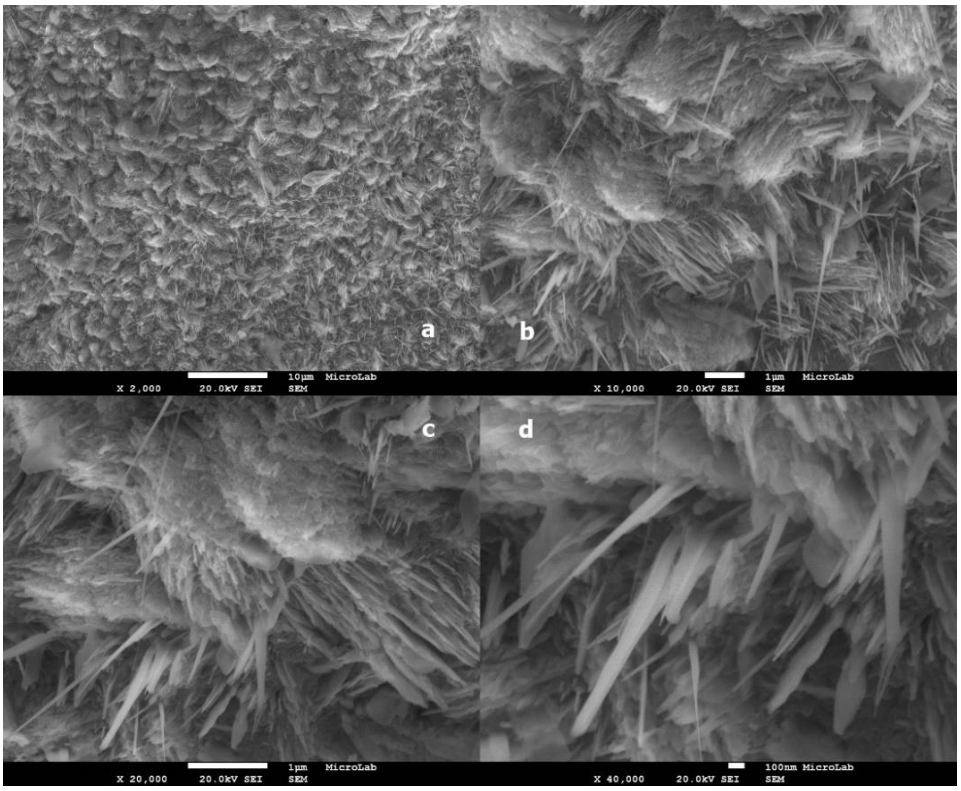

Figure 25. Secondary electron images from top view of the oxidized surfaced at 600°C for 48h taken at different magnifications.

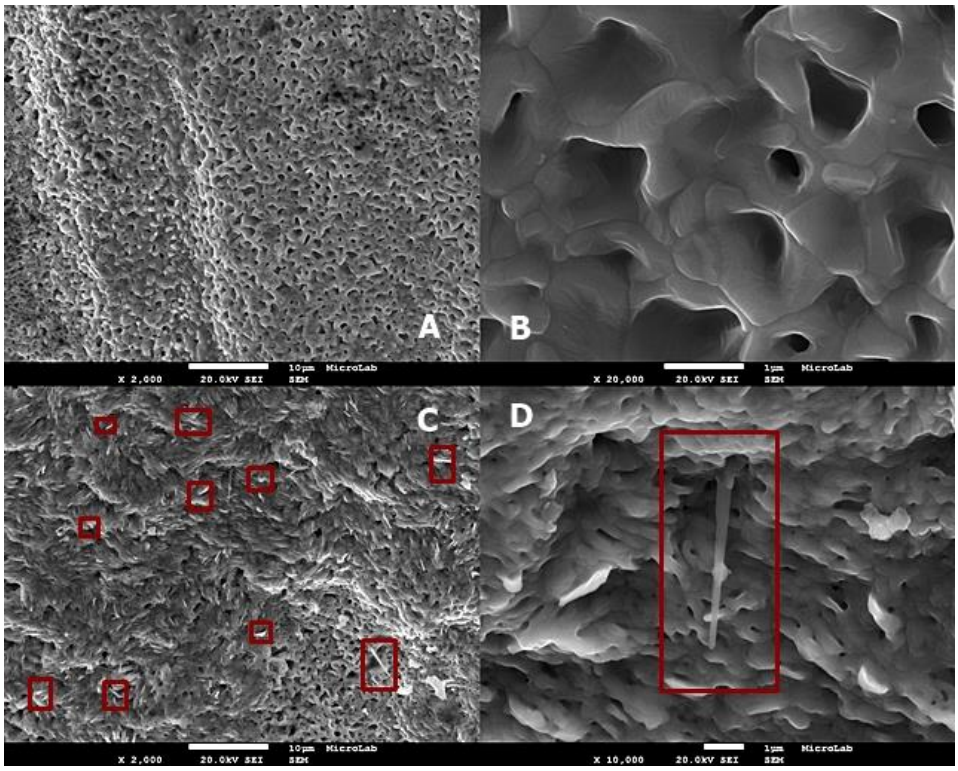

Figure 26. Secondary electron images from top view of the oxidized surfaced at 800°C for 48h taken in different regions and at different magnifications; A, B- porous area, C,D- porous area with needle-shaped structures.

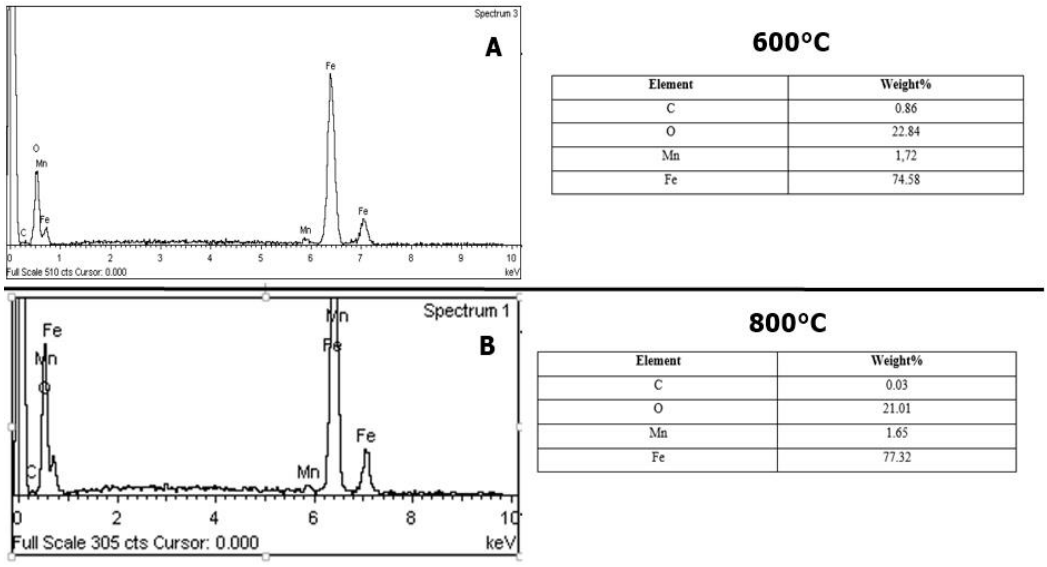

600°C

Element	Weight%
C	0.86
O	22.84
Mn	1,72
Fe	74.58

800°C

Element	Weight%
C	0.03
O	21.01
Mn	1.65
Fe	77.32

Figure 27. EDS analysis with elemental composition for samples oxidized at 600°C (A) and 800°C (B) for 48 h.

In the corresponding EDS analysis, the presence of iron-oxygen compounds were confirmed as shown in Figure 27 and 29. It can be concluded, that whatever the oxidation temperature both structures are enriched in iron and oxygen. Unfortunately, the Fe/O ratio was not sufficient to confidently determine which of the iron compounds represented the corrosion products in the tested systems due to the fact that the Fe/O ratios of the products were varied; yet it seemed to be in the range of most of the standard iron oxides. For this reason, the ferrous oxides were searched using a more detailed technique.

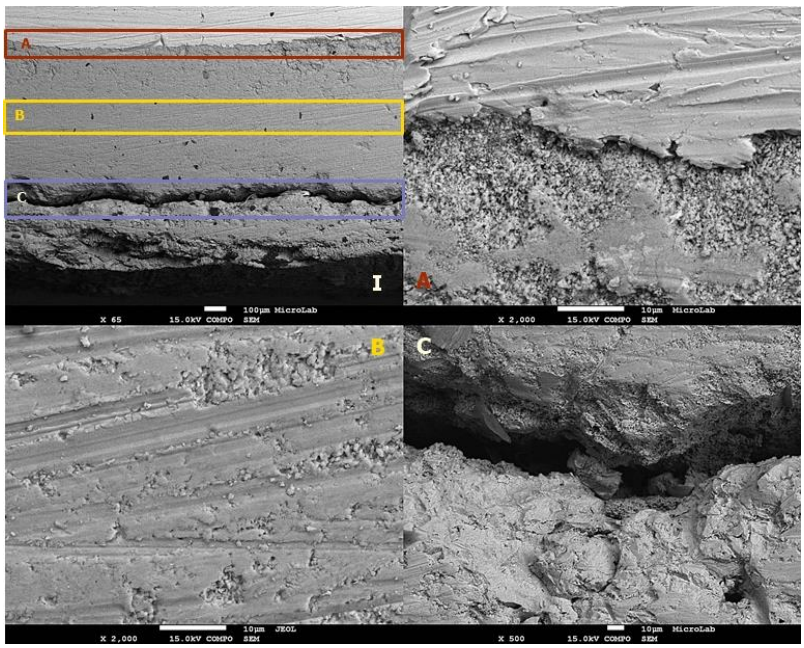

Figure 28. Backscattered electron images of cross-sections of oxidation products formed during oxidation at 800°C for 48h; I- overall view, A- interface metal-metal oxide, B- middle region of the film growth, C- crack region.

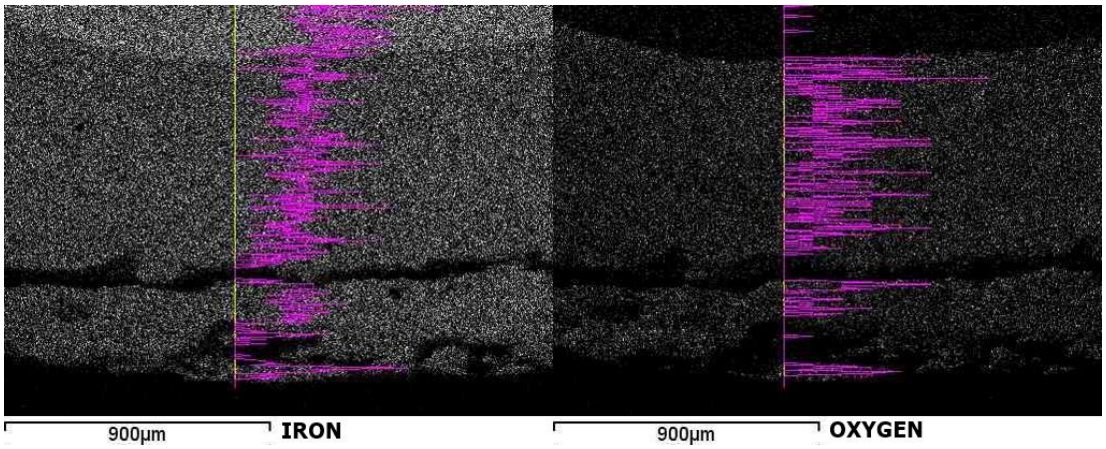

Figure 29. EDS mapping corresponded to the backscattered images of cross-sections analysis at 800°C for 48h.

The conclusions from SEM/EDS analyses are in good agreement with the results from Raman spectroscopy, which confirmed the presence of two iron oxides: Fe_2O_3 at both temperatures (600 and 800) and Fe_3O_4 found only at 800°C in the cross section measurements. The possible existence of an innermost layer composed of FeO could not be confirmed.

The Raman spectrum from the surface of the specimens oxidized at 600 and 800°C revealed several strong bands indicated in Figure 30 which correspond to α-Fe_2O_3. Comparing the two spectra patterns, the relative intensity of the peaks is changed. The hematite peaks for 800°C decreases whereas those of 600°C increases. In addition, the line widths of all peaks narrow as the temperature increases. Both indicate either the growth of the particle sizes and/or an enhancement of the crystallinity of the detected phase. The latter one is related to antiferromagnetic transition of Fe_2O_3 at 675°C [41]. The iron oxide transformation creates elevated stresses in the structure of the material. As a result a secondary recrystallization takes place, which induces texture in the as formed structure. This can, also explain partially the differences between the surfaces observed previously in SEM images.

Raman characterizations performed on the cross-section oxidised at 800°C (Figure 31) confirmed the presence of hematite in the regions indicated as 1 and 3 in Figure 31, where the scale was found without many variabilities (pores and voids). Moreover, in the area close to the crack where the internal layer was exposed, existence of another iron oxide with intense peaks at 660 cm^{-1} as well as small one at 530 cm^{-1} was revealed. Both of them are close to the reference peaks of magnetite (665 cm^{-1} and 527 cm^{-1}).

Detection of just the two iron oxide compounds: Fe_2O_3 and Fe_3O_4 can be explained by iron diffusion through vacancies attributed to FeO microstructure and the presence of oxygen at high concentration in the outer scale layers [31]. This leads to the formation of thicker magnetite and hematite layers above wüstite. Thus, the last one cannot be detected, if not enough penetration depth of the laser beam is used. Another possible explanation comes from the temperature influence on wustite behaviour. According to literature, during cooling from the oxidation to room temperature, this phase is not stable

and can transform into magnetite. Magnetite precipitates on the wüstite due to saturation of oxygen [45]. This precipitation can further complicate the distribution of the phases within the scale, so that FeO cannot be detected by Raman spectroscopy.

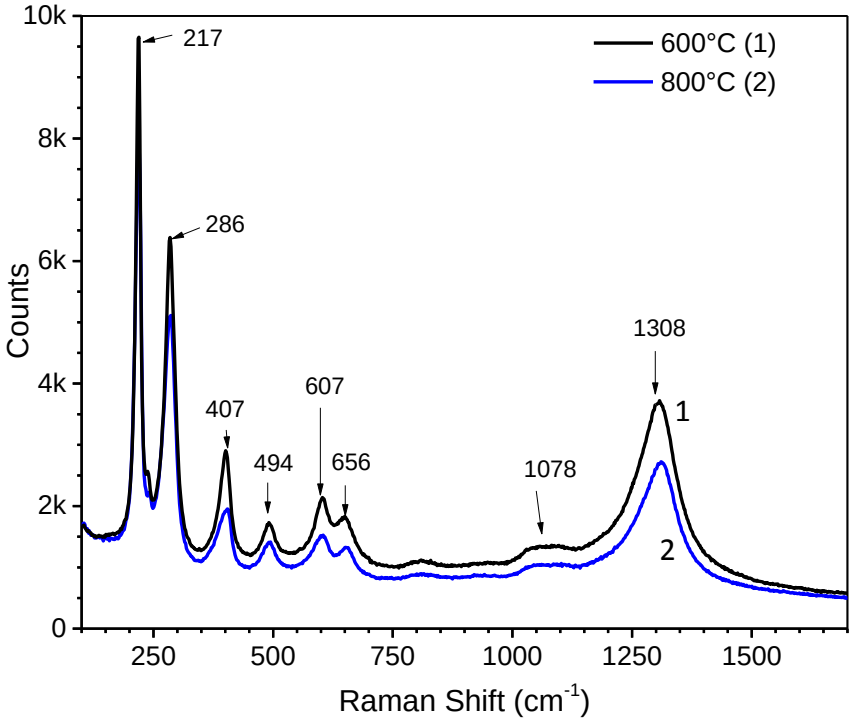

Figure 30. Raman spectra from top views of the samples oxidized at 600°C and 800°C for 48h.

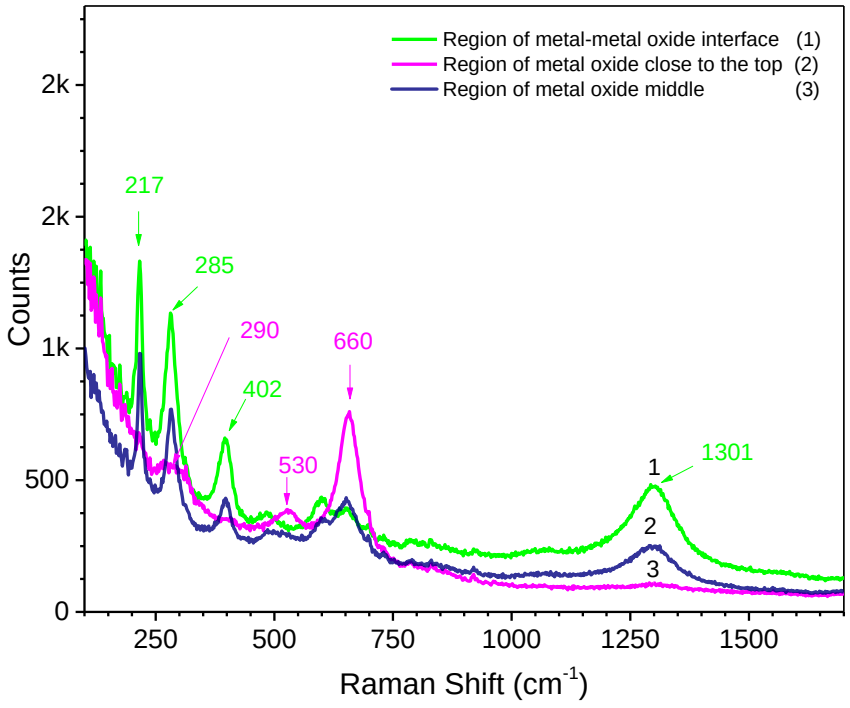

Figure 31. Raman spectra from different regions in cross-section of the sample oxidized at 800°C for 48h.

Table 5. Raman wavenumbers and assignments of the formed iron oxides after oxidation in air at 600 and 800°C [45,50,51]

Compound	Pure oxide (cm^{-1})	Experimental (cm^{-1}) Figure 30	Experimental (cm^{-1}) Figure 31
Hematite			
	225	217	217
	247	-	-
	292	286	285
	406	407	402
	495	494	490
	610	607	607
	660	656	650
	822	-	-
	1077	1078	-
	1300	1308	1301
Magnetite			
	298	-	290
	540	-	530
	668	-	660

6.2 Oxidation in presence of KCl

6.2.1 Mass change and micrographic analysis of the surface

The mass change determination was based on metal loss calculated after dissolving the remnants of salt on the surface with distilled water. The results revealed an important mass loss. The results are depicted in Figure 32 as mass change per surface area, with an error scale. The mass loss changes ranged from 42 mg/cm^2 to 59 mg/cm^2 and 72 mg/cm^2 to 92 mg/cm^2 at 600 and 800°C respectively depending on exposure time, to even 1000 mg/cm^2 at 1000°C. These losses occurred because surface scales tended to spall or to dissolve and became larger as temperature and time increased [46]. This effect is opposite to the one observed for oxidation in air and is consequence of the much more aggressive environmental conditions in the presence of the molten salt.

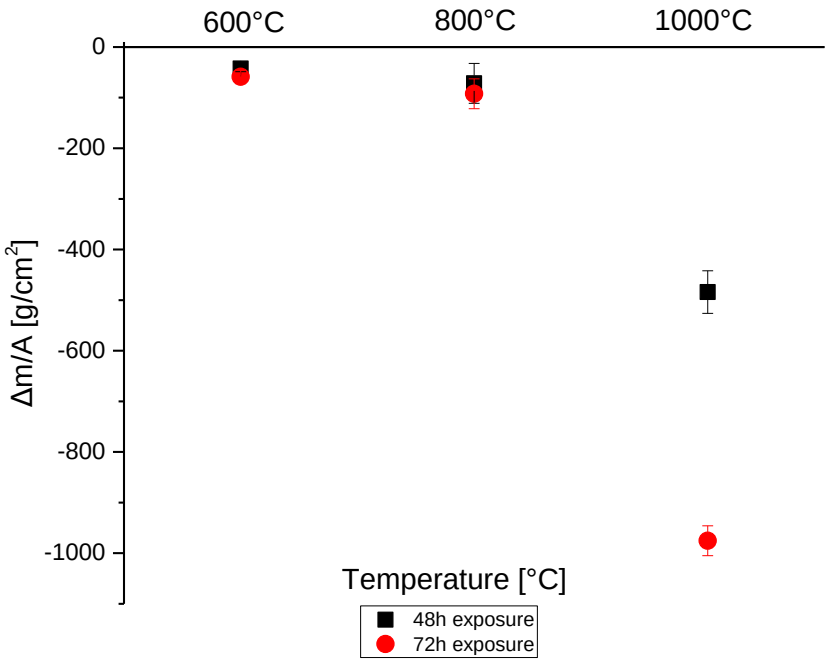

Figure 32. Mass loss per unit area (Δm/A) as a function of temperature of P235GH carbon steel during non-isothermal oxidation in presence of KCl.

A visual comparison of the effect of salt and its melt on the adhesion of the scales is presented in Figure 33. The surface obtained at the lowest oxidizing temperature, after 48h of exposure, was irregular with some deposits presented on the top. Those are similar to the ones observed in the previous oxidation experiment at the same temperature. However, it is clearly seen that presence of KCl disrupted the flaky structure. Further increase in the exposure time resulted in a more uniform surface, revealing evidences of corrosion - black regions, indicating scale spallation. It is suggested that in these conditions two opposite forces may arise on the steel surface. The oxygen helps in building and/or repairing the oxide scales, whilst the aggressive salt attacks the weakest areas in the film, thus assisting the corrosion process. Rising the temperature from 600°C to 800°C resulted in the formation of salt crystals either trapped in the scale (as presented for the exposure of 48h) or covering the whole surface when the duration of test increased. This was expected, since the experiment was carried out above the melting temperature of KCl (770°C). When the temperature exceeded this point, part of KCl started melting and destroying the scale. This interaction could result in the formation of volatile species ($FeCl_2$, or FeO_2Cl_2), which evaporated and condensed on the wall of the reaction tube exposing the metal beneath and promoting the corrosion attack [47]. The vaporisation of chlorine compounds also occurred at 1000°C, however the temperature applied caused severe material degradation and the result was that the metal surface was partially dissolved as shown in Figure 33E and 33F. The powder found in the pots after experiment indicating the significant mass loss was additionally examined in further analyses.

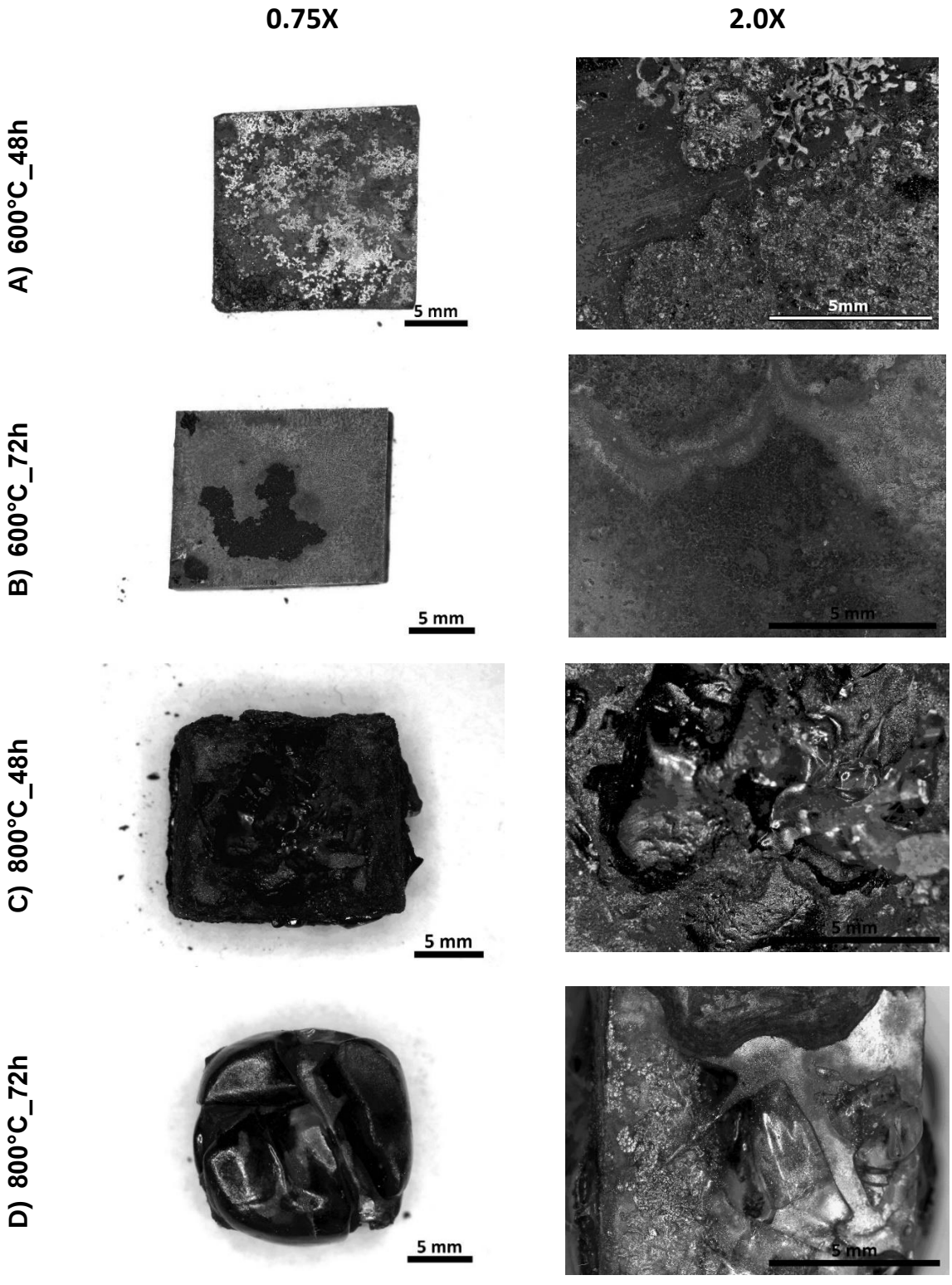
0.75X
2.0X
A) 600°C_48h
B) 600°C_72h
C) 800°C_48h
D) 800°C_72h
5 mm
5mm

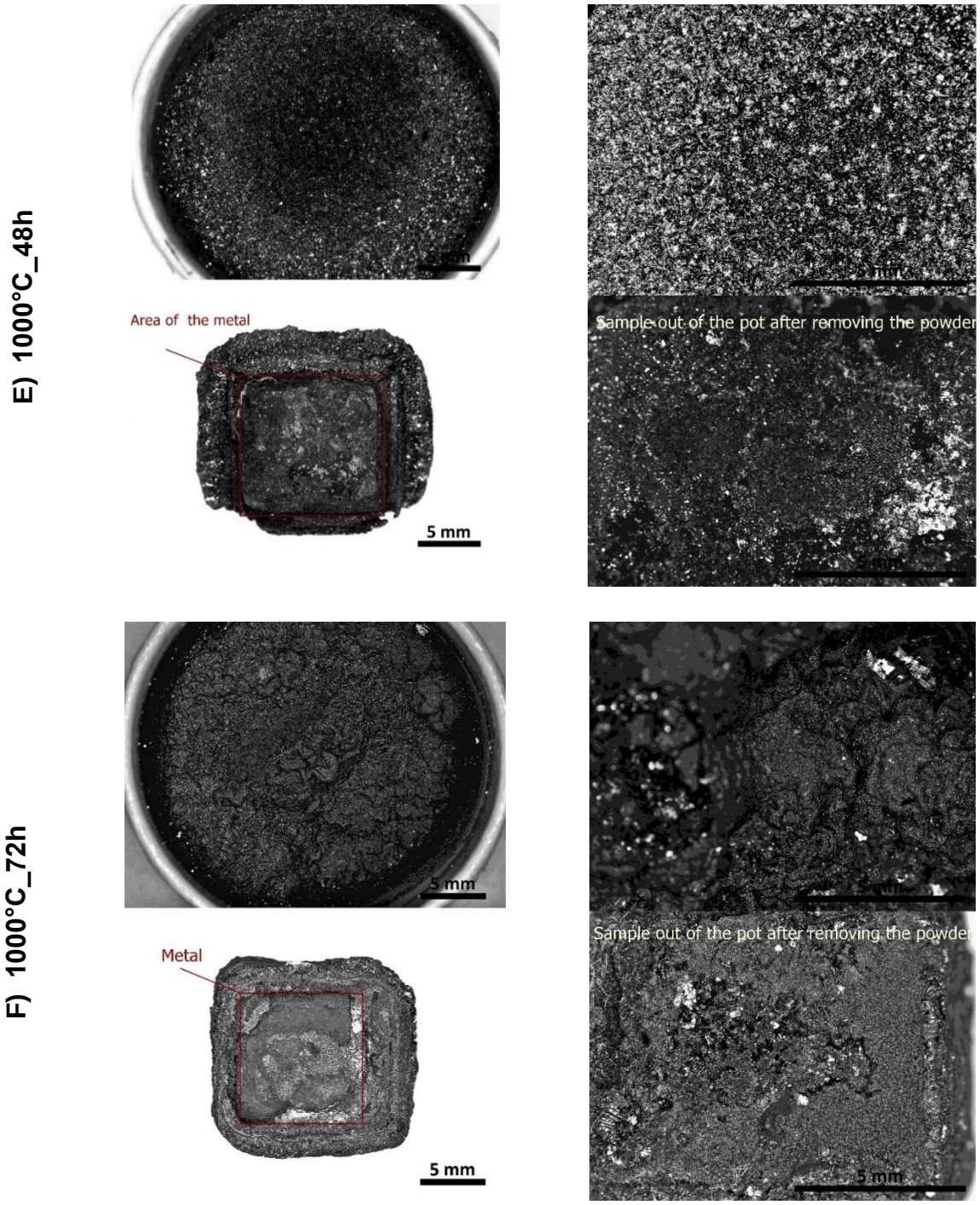

Figure 33. Optical macrographs showing the carbon steel after 48h and 72h of exposure in presence of KCl at selected temperatures. The images were taken at 0,75X (left) and 2,0X (right) magnifications.

6.1.2 Morphological and chemical identification of the scales

The morphology of the surface after aggressive salts attack is a vital part of materials evaluation in corrosion studies. The scale identification was done for the sample oxidised at 800°C after 48h and on the powders collected from the sample oxidised at 1000°C during the same exposure time.

SEM micrographs of several representative cross-sections taken at 800°C when the oxide scale was still attached are shown in Figure 37 The highly irregular structure revealed the presence of voids, cracks and pits. This is in contrast with the behaviour observed for the samples oxidised in air (Figure 28), where a continuous, and relatively smooth layer of iron oxides was seen at the carbon steel-oxide interface. It was found that the cracks were filled with KCl (Figure 34D) suggesting that a flux mechanism took place. It was additionally confirmed by EDS analysis (Figure 35 and 36), which detected the presence of both salt components as well as other elements, such as: iron, oxygen, magnesium etc.

In general, the salt attacks the oxide scales and cracks it. Once the protective iron oxide is fragmented and becomes non-protective, the chloride compound accelerates the corrosive attack on the steel. The effect of molten salts is similar since it hinders the formation of protective layer [47]. These processes resulted in layers which are non-continuous, non-adhesive and similar to the ones observed in the SEM images.

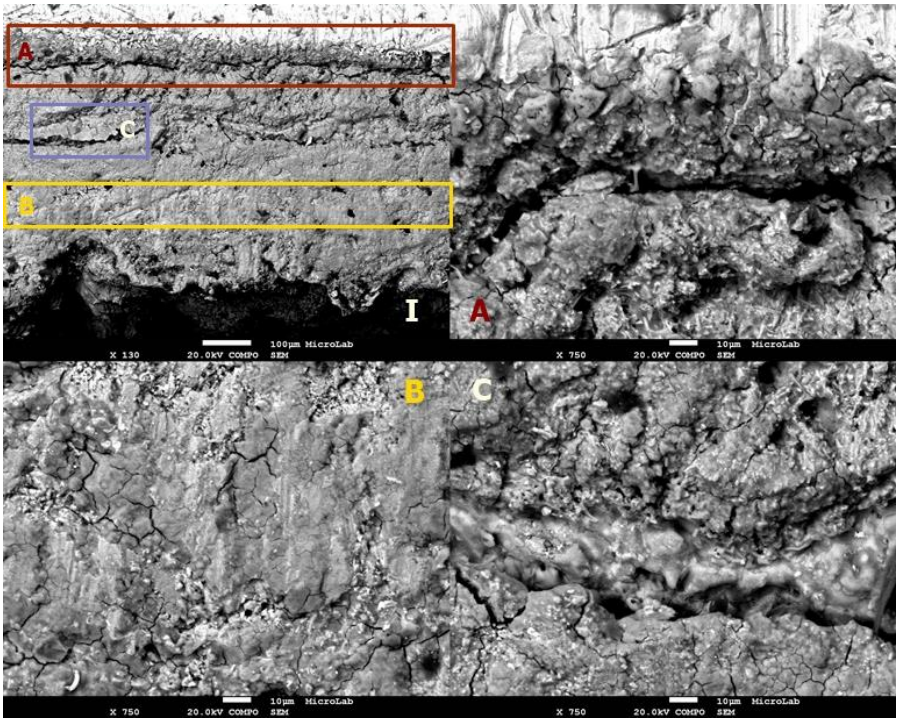

Figure 34. Backscattered electron images of cross-sections of surface after oxidation in presence of KCl at 800°C for 48h; I- overall view, A- interface metal-metal oxide, B-region of bulk film close to the surface, C- crack region filled with KCl.

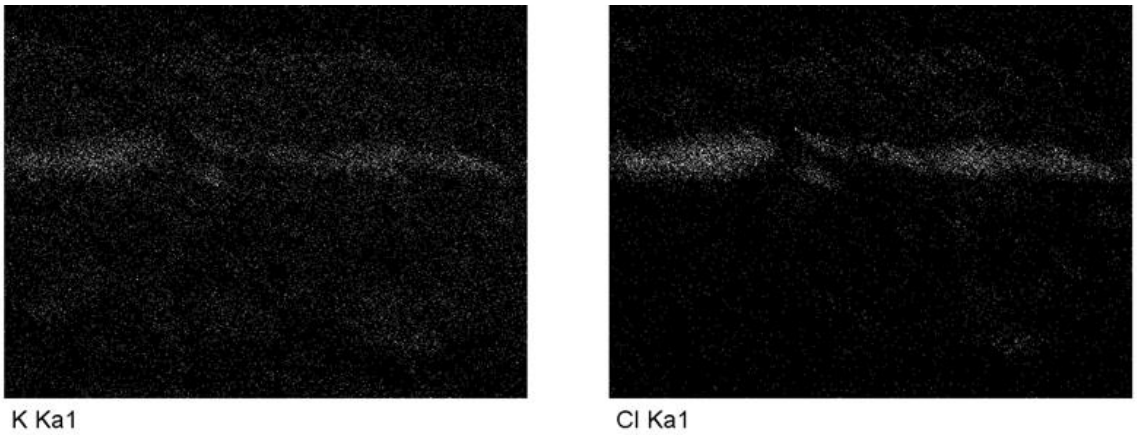

Figure 35. EDS mapping from the region of crack.

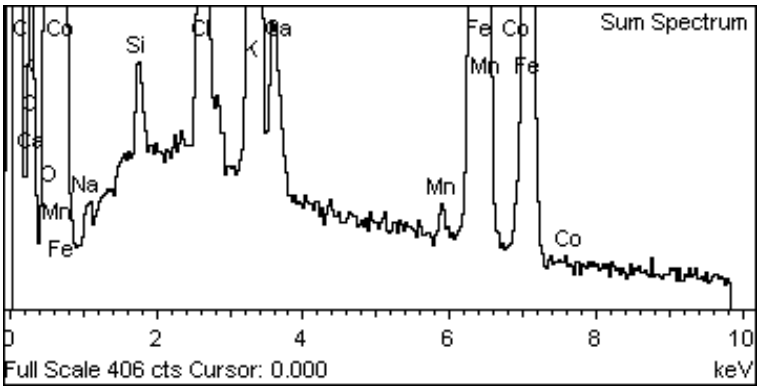

Figure 36. EDS analysis for sample oxidized at 800°C for 48 hours.

Supplementary analysis of the powder products obtained after 48 h at 1000°C show interesting findings. For this reason it was decided to include these micrographs along with chemical composition in this section. Optical images obtained previously depict the loosen structure of corrosion products, where the shiny particles were easily distinguished from the black matter. The first ones were found as smooth irregular crystals (Figure 37A), while the nature of the latter was amorphous (Figure 37B). EDS spot analysis was performed on the two points marked in Figure 38. Interestingly, both of the structures consisted of just two elements: iron and oxygen. Although the composition is similar, the Fe/O ratio varies indicating different compounds, which were identified by Raman. Absence of K or Cl only confirmed their complete evaporation from the surface as suggested in previous section.

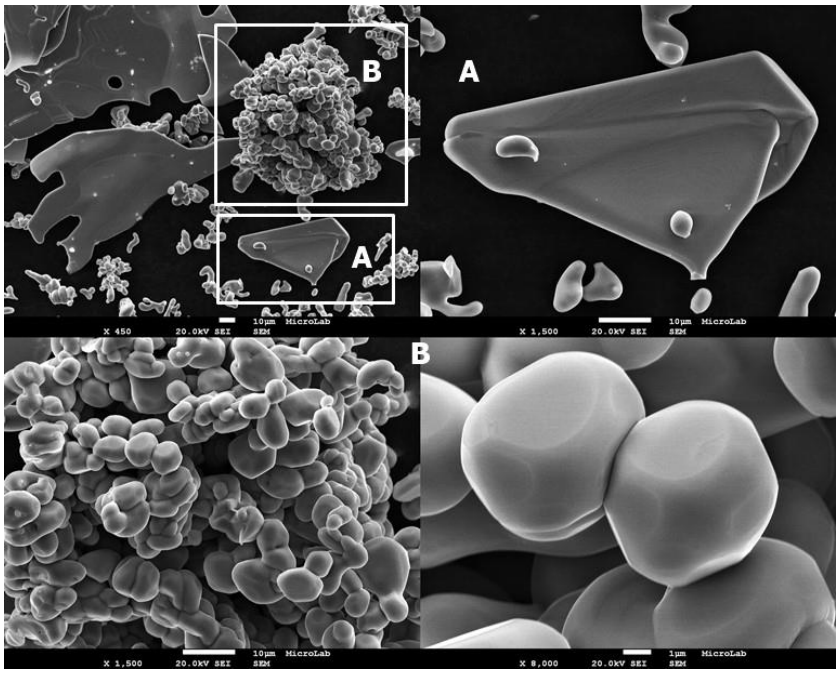

Figure 37. Secondary electron images of powder product obtained after 48h at 1000°C; A – phase with big dark and smooth crystals; B – phase with irregular crystallinity presented at different magnifications.

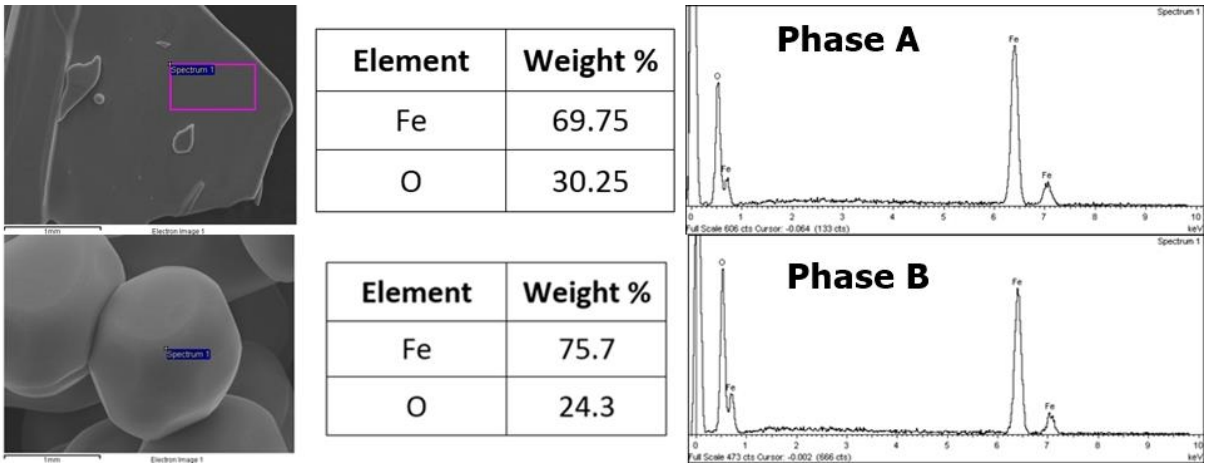

Figure 38. EDS Analysis of powder product obtained after 48h at 1000 °C; phase A – big dark and smooth crystals; phase B – amorphous black filling.

Again, the chemical composition of the surfaces examined with SEM were subsequently investigated by Raman spectroscopy to obtain a comprehensive picture of the corrosion products formed. Figure 40 shows the spectra obtained at different points on the surface of the sample oxidized at 600°C for 48h. Their characteristics differed in intensity, but were the same in terms of wavenumbers, and could be assigned to the hematite spectrum. In general, it can be concluded that at this temperature the salt attack is not that severe as observed at 800°C, since no other compounds were detected and the spectrum was comparable to the one obtained for the sample oxidised in air. Contrarily, the spectra obtained at 800°C (Figure 41) weren't similar to any known, however some bands were assigned to the presence of KCl (285 cm^{-1} and 1500 cm^{-1}) and magnetite (530 cm^{-1} and 670 cm^{-1}). The rough peaks

between 700 and 900 cm^{-1} can confirm the flux mechanism where melted salt disturbed the growth of the internal oxide layer and dissolved the outermost one, so that the hematite peaks could not be found in the examined region. However its presence was confirmed in cross-sections characterisation (Figure 41). The spectrum from the area close to the sample edge revealed several different features compared to the spectra from the middle region and oxide-metal interface. Analysing the whole graph, the shifting of the characteristic bands of hematite between 200 and 600 cm^{-1} and presence of characteristic peaks of magnetite, along with the appearance of interferences between 700 and 900 cm^{-1} can be an indication of the influence of KCl on the iron oxide. It may happen that chloride compounds such as $FeCl_2$ or $FeCl_3$ would be found, but all of these were either evaporated or existed as discrete layers which are not detectable with this technique. Presence of hematite, confirmed at each tested temperature, was also found at 1000°C (Figure 42) in the form of big dark and smooth crystals (phase A). In the case of shiny particles (phase B) the two peaks (215 cm^{-1} and 270 cm^{-1}) can match with the hematite's ones, the absence of any others can be related to the irregular crystallinity of iron-oxide compound observed in SEM images.

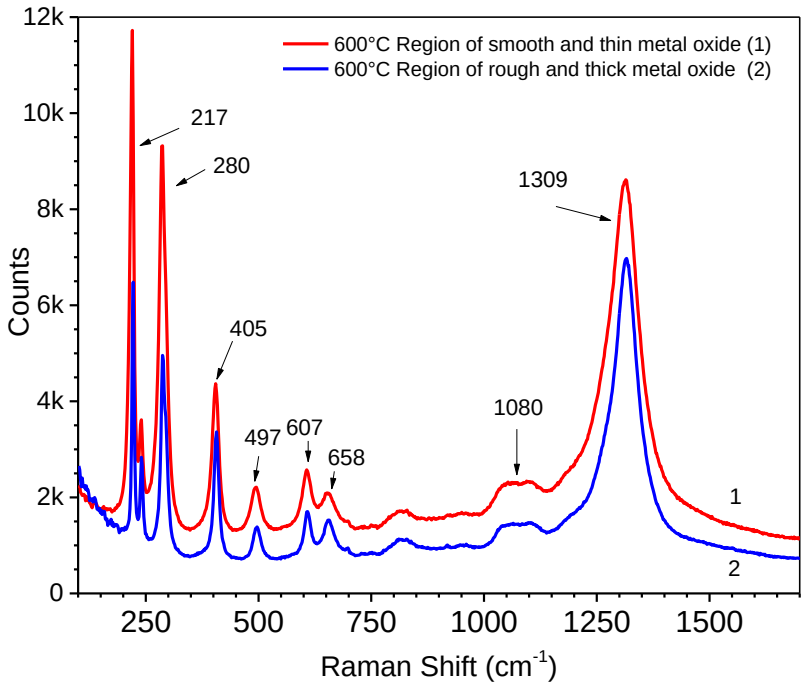

Figure 39. Raman spectra from different regions of the surface oxidized in salt at 600°C for 48h.

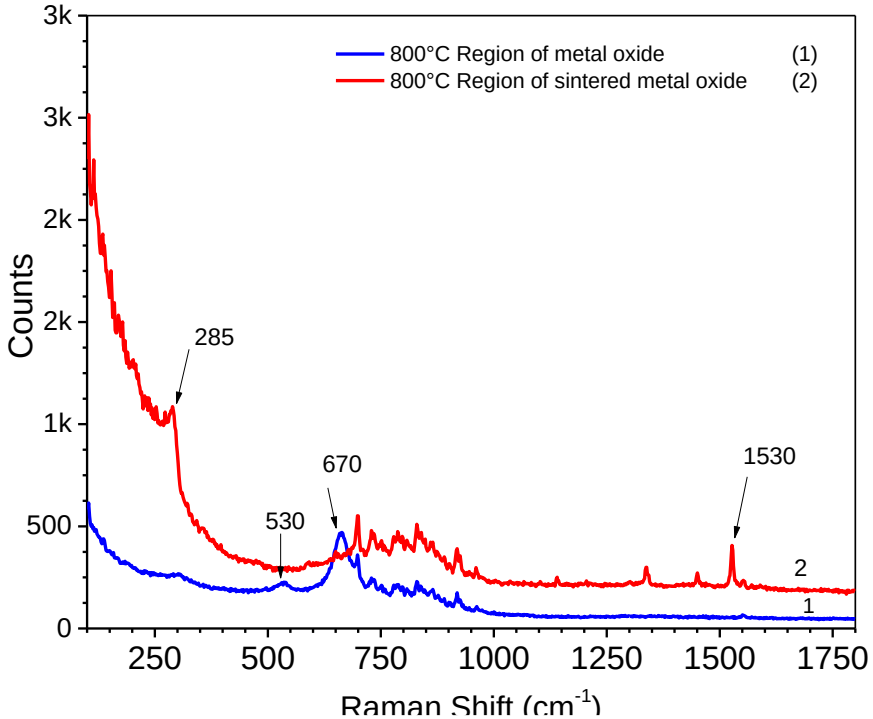

Figure 40. Raman spectra from different regions of the surface oxidized in salt at 800°C for 48h.

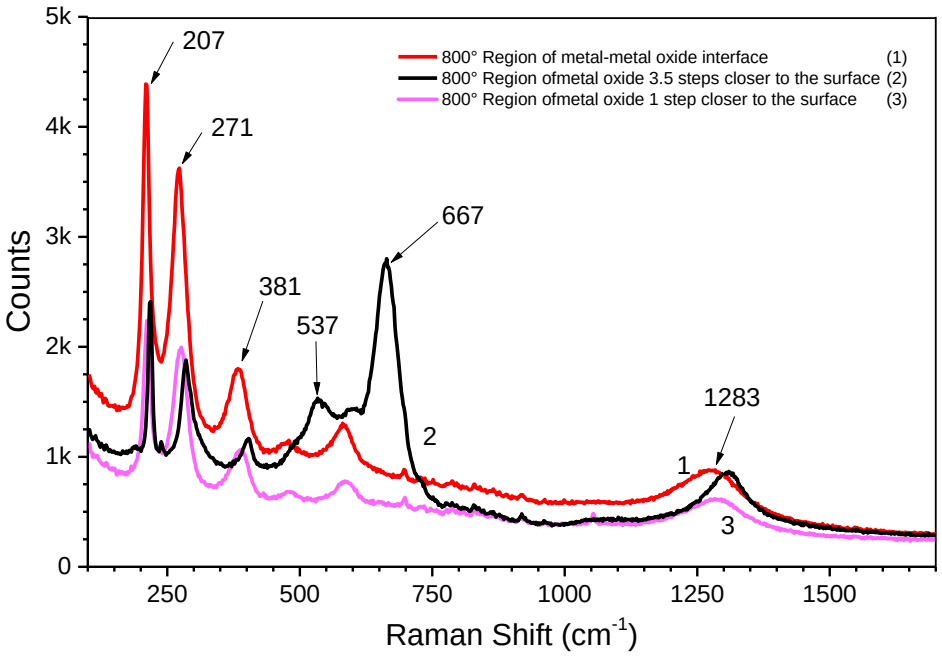

Figure 41. Raman spectra from different regions in cross section of the sample oxidized in salt at 800°C for 48h.

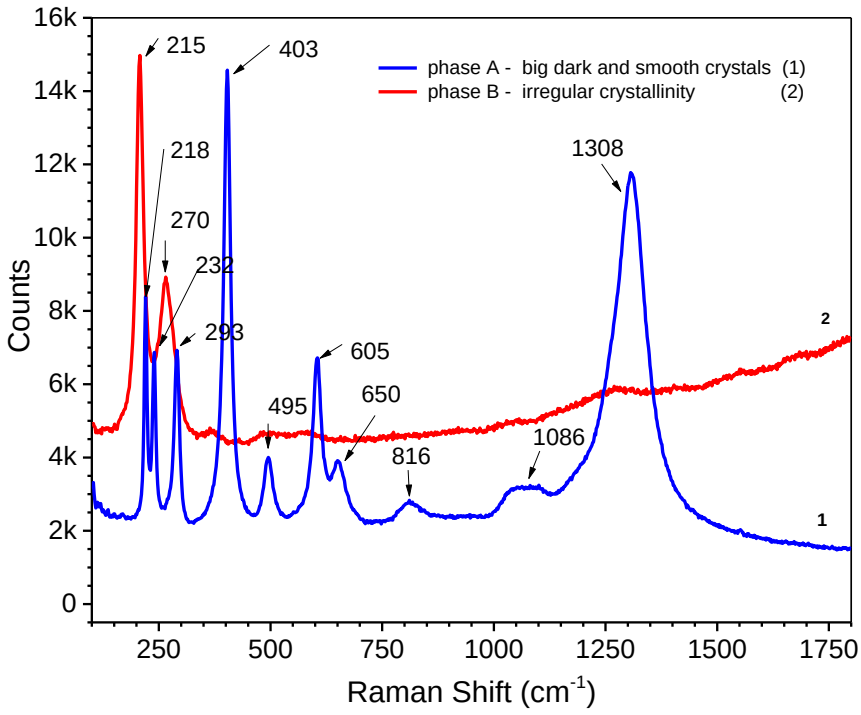

Figure 42. Raman spectra of powder product after oxidation is salt at 1000h for 48.

Table 6. Raman wavenumbers and assignments of the formed iron oxides after oxidation in salt at 600 800°C and 1000°C [45,50,51].

Compound	Pure oxide (cm^{-1})	Experimental (cm^{-1}) Figure 39	Experimental (cm^{-1}) Figure 40	Experimental (cm^{-1}) Figure 41	Experimental (cm^{-1}) Figure 42
Hematite					
	225	217	-	207	215/218
	247	-	-	-	232
	292	280	-	271	293
	406	405	-	381	403
	495	497	-	475	-
	610	607	-	-	605
	660	658	-	-	650
	822	-	-	-	816
	1077	1080	-	-	1086
	1300	1309	-	1283/1308	1308
Magnetite					
	298	-	-	-	-
	540	-	530	537	-

	668	-	660	667	-
Potassium chloride					
	285	-	290	-	-
	774	-	-	-	-
	1564	-	1530	-	-

6.3 d.c. Polarization measurements

In this method the corrosion resistance of the scales formed in both experiments was measured in the presence of an electrolyte (alkaline solution) together with the corrosion potential (Ecorr).

The d.c. polarisation curves obtained from oxidation in air highlighted two distinct behaviours that occurred regardless the surface conditions of the steel as shown in Figure 43 and 44. The samples oxidized at 600°C and 800°C are characterised by more negative corrosion potentials (Ecorr), thus being slightly cathodically polarised. Contrarily, the specimens from the oxidation tests up to 1000°C are characterised by much more positive corrosion potential (Ecorr) and lower current densities compared to that observed at lower temperatures. These samples showed an important anodic polarization effect.

Generally, the corrosion of steel in alkaline media is described by specific reactions that shall proceed at the same rate. One is the anodic reaction and consists of an oxidation of the metal so that it changes from the metallic state to an ionic state: $Fe \rightarrow Fe^{2+} + 2e$, while the cathodic reaction occurs at different sites from the anodic one, as follows: $O_2 + 2H_2O + 2e \rightarrow 4OH^-$. In alkaline solution, the reduction of oxygen only occurs in the potential range where the iron oxides is reduced [48]. It means that at negative potential, where the activity of cathodic reaction is higher than at positive one, the metal is more susceptible to corrosion due to reduction of formed oxide layer. This leads to an increase in current density that was confirmed after oxidation at lower temperatures. The values of I_p (corrosion current) obtained with potentiodynamic tests for 600 and 800°C were lower than that the ones measured for the blank sample, which passivates in alkali solution, but higher than those observed up to 1000°C. It suggests that in some extent, the scale provides metal protection, but lower than expected. This correlates with the observations from optical and SEM micrographs, where the surface examinations indicated irregularities in the scales formed at 600 and 800°C that could lead to reduction of corrosion resistance and its variability, as observed for 600°C_48h and 800°C_72h. Contrarily, at elevated temperatures (Figure 44) the presence of a thicker and uniform scale formed after oxidation was confirmed by an important decrease in the anodic current density. This occurs only if a protective coating appears, requiring higher potential to be broken down. However not all samples up to 1000°C provided the same degree of steel protection. In case of one oxidized at 1100°C for 48h the protectiveness was diminished due to partially destroyed scale.

On the whole, the formed scale experienced little corrosion at low cathodic potential to no corrosion at higher anodic potentials. The latter is related to the thick oxide layer that is formed on the surface of the

metal and that inhibits corrosion. It becomes a barrier between the metal and the electrolyte and slows the anodic reaction because ions have low diffusivity in the oxide [49].

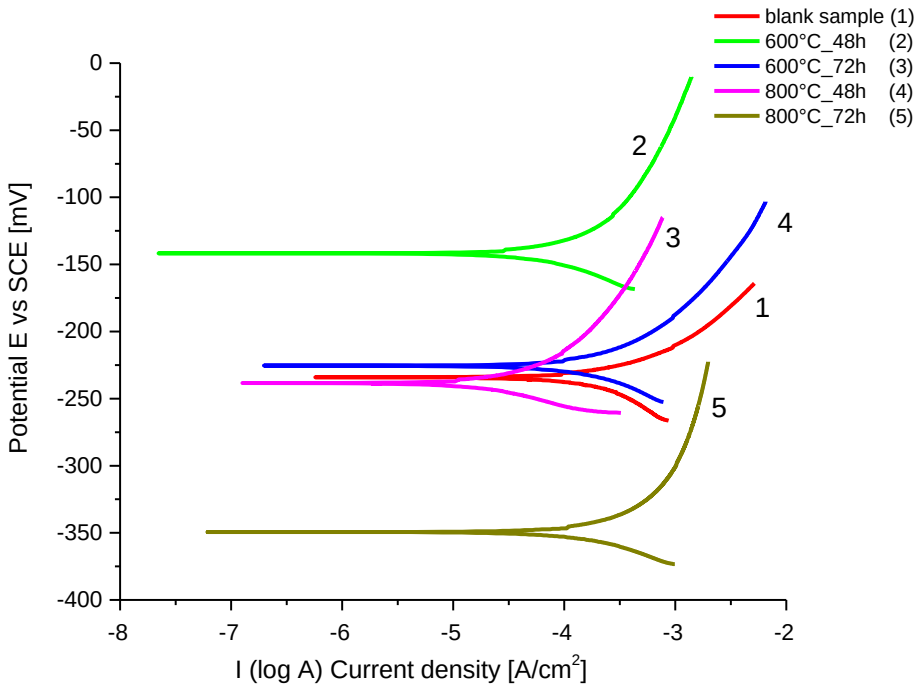

Figure 43. Polarisation curves of carbon steel samples oxidized at 600 and 800°C.

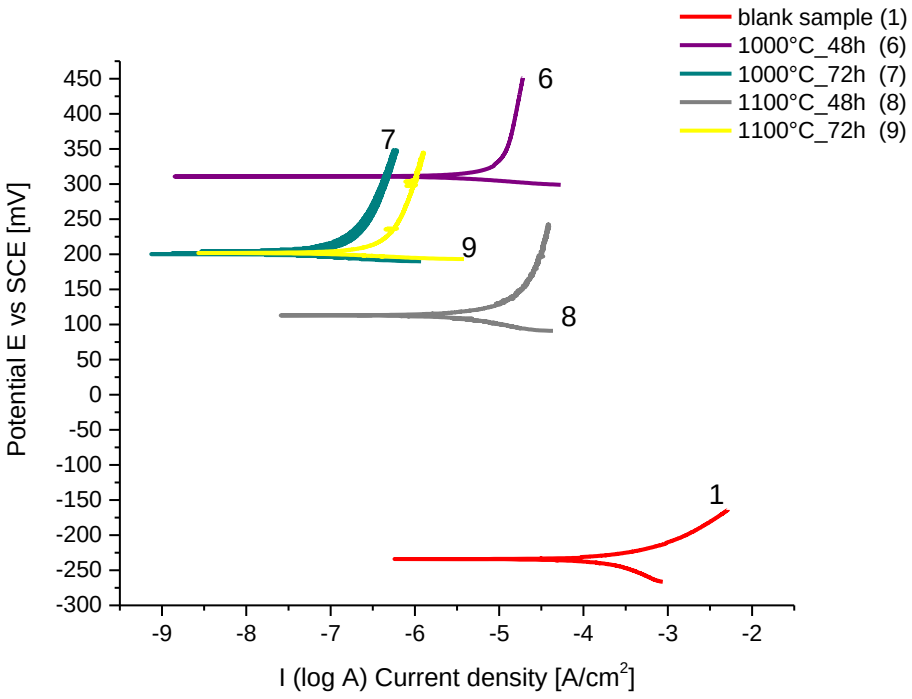

Figure 44. Polarisation curves of carbon steel samples oxidized at 1000°C and 1100°C.

Polarisation curves were also taken in an attempt to understand the corrosion behaviour of the samples oxidised in the presence of KCL and the results are depicted in Figure 45. The test performed on the sample oxidised at 1000°C for 72h could not be performed with reliability. It was noticed that the

corrosion potential shifted towards more negative (cathodic values) as the temperature increased, indicating some polarization effect on the cathodic reactions (oxygen reduction might became more difficult). Moreover, the current density increased significantly compared to the blank sample, revealing that the oxidised material is much more susceptible to corrosion. The thin passive film formed on raw steel in alkali solution had better anticorrosive properties compared to the surfaces exposed to the environment containing aggressive KCl regardless the temperature. The increase of the corresponding current densities with increasing temperature was the consequence of non-continuous and non-adherent scale formed in presence of the salt as was determined in previous analyses. On the other hand, traces of chlorides, trapped in the scales, in the presence of water and oxygen may contribute to further attack of the weak areas, increasing the corrosion activity and consequently to the increased anodic current densities. This results contrasts to the behaviour observed for the samples oxidise in air only, where the corrosion potential increased with rising temperature, resulting in lowered current densities revealing that a more protective scale was formed.

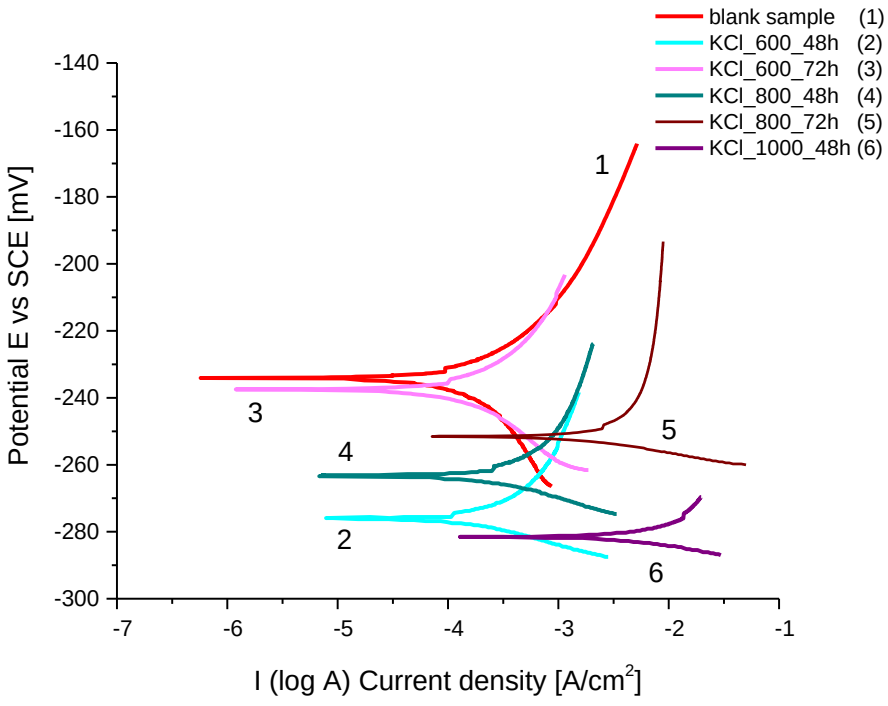

Figure 45. Polarisation curves of carbon steel samples oxidized in salt.

Conclusions

In this work the oxidation performance of carbon steel and scales formed on its surface during experiments conducted in different environments were analytically and electrochemically examined.

High Temperature Corrosion testing

The investigated steel exhibited two different performances depending on the reaction environment. When oxidised in air there was a relevant mass gain, while the reaction between oxygen and iron was disrupted by presence of KCl resulting in significant mass loss. Both experiments indicated non-linear mass changes with some deviations found above 1000°C and 800°C for first and second test, respectively. Those variations were related to severe conditions in which this type of steel does not operate without additional protection. Nevertheless, non-linearity of the oxidation rate suggested by the obtained results for the scales growth couldn't be fully confirmed due to the limited data obtained.

The samples oxidised in air, when exposed to higher temperatures and longer exposure time, evidenced scales that thicken and morphologies that changed from heterogeneous to uniform ones as result of an accelerated reaction between iron and oxygen. Contrarily, the scales formed during oxidation in salt tended to spall or to dissolve due to the aggressive species present. The scale dissolution was observed above the melting point of KCl (770°C). This interaction resulted in a highly defective morphology as revealed in the SEM micrographs. Several defects leading to material failure were also found in the experiments without salt, however their origin could be related to the mechanical work applied. Thus, the resistance of the steel can be altered in case where high temperature and mechanical stressing are introduced.

The structural and chemical examination of the scale formed at 600°C and 800°C in both tests, showed that the outer deposit was composed of Fe_3O_4 regardless the conditions. Cross sections measurements revealed the presence of Fe_2O_3 in inner layer at 800°C in every case. In this temperature, after oxidation in salt the flux mechanism was confirmed with KCl characteristic peaks found in cracked scale. Additionally at higher temperature (1000°C) the complete vaporisation of salt and consequently chlorides were suggested due to absence of any of its compound detected with EDS as well as Raman analysis.

Aqueous Electrochemical testing

The electrochemical experiments performed in aqueous media revealed some interesting and logical findings. The samples oxidised in air showed two distinct behaviours characterised by corrosion potentials more cathodic (600 and 800ºC) or more anodic (1000 and 1100 ºC) compared to the blank samples. The uniformity and protectiveness of the scales formed is thus distinct and more significant at higher temperatures. The scales formed at 1000 and 1100ºC provide an important barrier effect that protects the underlying steel from further corrosion in aqueous media typically found during cool down periods or when the boilers stop. It is worth to notice that this separation (corrosion potential changes), at the best of the author knowledge, was never reported before and thus, this result constitutes an

original finding. Oxidation in the presence of KCl definitely increases the corrosion susceptibility at any temperature. Both the corrosion currents and anodic currents increase significantly when chlorides were present in the oxidation process.

In summary, though mild steel can sustain high temperatures in air, its application in chloride-rich environment, typical for boilers, which use straw as a combustive material, can be hardly advocated.

Future work

In addition to the work already done, more measurements regarding oxidation kinetics should be conducted. Thermogravimetric analysis would give better insight of the corrosion rate and thereby proper kinetic model of corrosion occurring on carbon steel surface at selected conditions could be assessed. Furthermore detailed cross sectional analysis of the oxide scales with SEM and EDS as well as composition analysis employing different techniques would be performed on more samples in order to find out the reasons for some of the changes observed in corrosion behaviour. Surface examination should also be considered after electrochemical testing to see morphological changes in aqueous environment and further compare them to ones after air oxidation in different conditions. Generally, extended thermal analysis along with detailed studies on microstructural changes would solidify the results of this paper.

References

[1] http://www.europeanclimate.org/documents/Biomass_report_-_Final.pdf [accessed on 2nd May 2015]

[2] International Energy Agency: https://www.iea.org/topics/renewables/subtopics/bioenergy/ [accessed on 3nd May 2015]

[3] https://www.biomassthermal.org/resource/PDFs/Fact%20Sheet%203.pdf [accessed on 2nd May 2015]

[4] N. Bątorek-Giesa, B. Jagustyn, *Chlorine content in solid biomass used for power industry,* Ochrona Środowiska I Zasobów Naturalnych, (2009), 40, pp. 396-401

[5] F. Biedermann, I. Obernberger, *Ash-related problems during biomass combustion and possibilities for a sustainable ash utilisation,* Austrian Bioenergy Centre GmbH

[6] M.Hiltunen, V.Barišić, E. Coda Zabetta, *Combustion of different types of biomass in CFB boilers,* 16th European Biomass Conference, (2008)

[7] http://www.videncenter.dk/gule%20halm%20haefte/Gul_Engelsk/halm-UK02.pdf [accessed on 20th March 2015]

[9] T. Nussbaume, *Combustion and co-combustion of biomass: fundamentals, technologies, and primary measures for emission reduction,* Energy and Fuels, (2003), 17, pp. 1510-1521

[10] B.M. Jenkins, L.L. Baxter, T.R. Miles Jr., T.R. Miles, *Combustion properties of biomass,* Fuel Processing Technology, (1998), 54, 17-46

[11] W. Denisiuk, *Straw as fuel,* Inżynieria Rolnicza, (2009),110, pp. 83-89

[12] R. Riedl, J.Dahl, I. Obenberger, M. Narodoslawsky, *Corrosion in fire tube boilers of biomass combustion plants,* Proceedings of the international corrosion control conference, (1998), 90129

[13] X. Weia, U Schnellb, K. R.G., *Hein Behaviour of gaseous chlorine and alkali metals during biomass thermal utilisation,* Fuel, (2005), 84, 841–848

[14] http://www.biomasa.org/index.php?d=artykul&kat=52&art=48 [accessed on 30th March 2015]

[15] E.F Kristensen, J.K Kristensen, *Development and test of small-scale batch-fired straw boilers in Denmark,* Biomass and Bioenergy, (2004), 6, pp. 561-569

[16] P.Elliot, *Practical guide to high temperature alloys,* Material Performance (1990)

[17] A.C. Uzorh, *Corrosion Properties of Plain Carbon Steels,* The International Journal Of Engineering And Science, (2013), 11, pp. 18-24

[18]http://www.nickelinstitute.org/~/Media/Files/TechnicalLiterature/Castings_Stainless_Steel_and_Nickel_Base_11022.pdf [accessed on 25thJune 2015]

[19] J N. Dupont, *Welding of Nickel-Based Alloys for Energy Applications*, Supplement to the welding journal, (2014), 93, pp. 32-45

[20] http://www.bssa.org.uk/topics.php?article=71 [accessed on 19th April 2014]

[21] P.Elliot, *Choose Materials for High-Temperature Environments*, International 55th Annual Conference and Exhibition, (2001)

[22] https://en.wikipedia.org/wiki/Cast_iron [accessed on 19th April 2015]

[23] J. R. Davis, *Stainless steel*, ASM International Materials Park , (1999), pp.205-206

[24] http://www.alibaba.com/ [accessed on 24th June 2015]

[25] S. Mrowec, *Zarys teorii utleniania metali*, Katowice: Wydawnictwo Śląsk, (1971).

[26] R.Beith, *Small and micro combined heat and power (CHP) systems: advanced design, performance, materials and applications,* Woodhead publishing, (2011), pp. 96-101

[27] Iron and steel processing: http://www.jfe-21st-cf.or.jp/chapter_2/2b_1.html [accessed on 25th June 2015]

[28] B.S. Mitchell, *An Introduction to Materials Engineering and Science for Chemical and Materials Engineers 1st Edition,* John Wiley & Sons, (2004), pp. 183

[29] N. Perez, *Electrochemistry and Corrosion Science*, Springer US, (2004), pp. 316-317

[30] J.R. Davis, *ASM specialty handbook: Heat-resistant materials*, ASM International, (1997), pp. 37

[31] G.Y.Lai, *High-temperature corrosion and materials applications,* ASM International, (2007), pp. 11-19

[32] M. G. Fontana, *Corrosion Engineering*, McGraw-HILL ,3rd edition, (1987)

[33] H.P. Nielsena, F.J. Frandsena, K. Dam-Johansena, L.L. Baxterb, *The implications of chlorine-associated corrosion on the operation of biomass-fired boilers,* Progress in Energy and Combustion Science, (2000), 26, pp. 283–298

[34] T. M. Mitrovski, *Thermodynamical analysis of (Fe-O-Cl) system*, Proceedings of 3rd BMC, (2003), pp.75-79

[35] G.J.Janz, R.P.T. Tomkins, C.B Allen, , J.R. Downey, Jr., G.L.Gardner, U.Krebs, S.K.Singer, *Molten salts: chlorides and mixtures,* J. Phys. Chem. Ref. Data **4**, 871, (1975).

[36] P. M. Stephan, *Refractory tile installation - mortar or no mortar*?, 12th North American Waste to Energy Conference, (2004), pp. 129-136

[37] M. Oksa, P. Auerkari, J. Salonen, T. Varis, *Nickel-based HVOF coatings promoting high temperature corrosion resistance of biomass-fired power plant boilers,* Fuel Processing Technology, 5, (2014), 12, 236–245

[38] A. J. Bard, L. R. Faulkner, *Electrochemical Methods, Fundamentals and Applications*. John Wiley & Sons, New York, (1980)

[39] M.S.J. Hashimi, *Comprehensive material processing*, Elsevier, (2014), pp. 190

[40] http://www.masteel.co.uk/p235gh.htm [accessed on 2nd July 2015]

[41] G. Vourlias, D. Chaliampalias, T.T. Zorba, E. Pavlidoub, P. Psyllaki, K.M. Paraskevopoulos, G. Stergioudis, K. Chrissafis , *A combined study of the oxidation mechanism and resistance of AISI D6 steel exposed at high temperature environments*, Applied Surface Science, (2011), 257, pp. 6687–6698

[42] V.K. Tolpygo, D.R. Clarke, *Spalling failure of α-alumina films grown by oxidation: I. Dependence on cooling rate and metal thickness,* Materials Science and Engineering, (2000), 278, pp. 142–150

[43] S. Birosca, G. D. West and R. L. Higginson, *Microstructural investigation of the oxide scale on low carbon steel,* Metal, (2005)

[44] M.Schutze, *Mechanical-properties of oxide scales*, Oxidation of Metals, (1995), 44, pp. 29-61

[45] M.A. Legodi, D. de Waal, *The preparation of magnetite, goethite, hematite and maghemite of pigment quality from mill scale iron waste, Dyes and Pigments*, (2007) 74, pp. 161-168.

[46] R. W. Bradshaw, W. M. Clift, *Effect of chloride content of molten nitrate salt on corrosion of A516 carbon steel*, Sandia National Laboratories, (2010)

[47] B.N.Popov, *Corrosion engineering: Principles and Solved Problems,* Elsevier, (2015)

[48] L. Feng, H. Yang , Fuhui Wang *Effect of an Imidazoline Derivative on the Protection Performance of Oxide Film Formed on Carbon Steel in Saturated $Ca(OH)_2$ Solution,* Int. J. Electrochem. Sci.,(2012), 7, pp. 4064 – 4077

[49] J.R Davis*, Corrosion Understanding the Basics*, Materials Park: ASM International, (2000)

[50] J. Dunnwald and A. Otto, Corrosion Science, (1989), 29, pp. 1167–1176

[51] http://rruff.info/Hematite/X050102; http://rruff.info/magnetite/display=default/R060191 [accessed on 19th July 2015]